Domenech Carbo, MT.; Mai-Cerovaz, C.; Doménech-Carbó, A. (2022). Application of focused ion beam-field emission scanning electron microscopy-X-ray microanalysis in the study of the surface alterations of archaeological tin-glazed ceramics. Ceramics International. 48(10):14067-14075. https://doi.org/10.1016/j.ceramint.2022.01.292

Application of focused ion beam-field emission scanning electron microscopy-X-ray microanalysis in the study of the surface alterations of archaeological tin-glazed ceramics

María Teresa Doménech-Carbó[a*], Carolina Mai-Cerovaz[a], Antonio Doménech-Carbó[b]

[a]Institut Universitari de Restauració del Patrimoni, Universitat Politècnica de València, Camino de Vera s/n, 46022 Valencia, Spain
[b]Departament de Química Analítica, Universitat de València, Avda. Dr Moliner s/n, 46100 Burjassot, Spain

Corresponding author: tdomenec@crbc.upv.es

Keywords: archaeological tin-glazes, FIB-FESEM-EDX, FTIR spectroscopy, optical microscopy, glaze corrosion process

Abstract

The historical evolution of the manufacturing technique of tin-glazed ceramics since ancient times as well as the differences in materials and manufacture according to their provenance are subjects that have attracted the attention of many scientists and, consequently, abundant archaeometrical studies can be found in the specialized literature. Nevertheless, a lesser number of studies aimed at the characterization of the alterations undergone by archaeological glazes has been reported. This work describes some unusual alteration processes found in tin-glazes depending on the environmental conditions to which they were subjected during centuries. For this purpose, focused ion beam-field emission scanning electron microscopy-X-ray microanalysis (FIB-FESEM-EDX), an advanced instrumental technique for surface analysis, has been used for the first time, complementarily to optical microscopy (OM), FESEM-EDX and Fourier transform Infrared spectroscopy (FTIR). In particular, the FIB-FESEM-EDX has shown the morphological and compositional changes that have taken place in the surface and subsurface of the glazes at the nanoscale. The analyses carried out have shown that differential corrosion processes occur depending on the environment surrounding the piece. In the buried glazes an outer lamellar corrosion layer due to humidity-dryness cycles is found, similarly to that found in buried glasses. This layer is placed over a thinner gel layer silica-rich. The absence of a corrosion layer is observed in submarine glazes that, in contrast, have undergone an unusual and selective erosion of the glaze matrix due to the silicification metabolism of diatoms. A thin outer corrosion layer formed by precipitated corrosion products and unspecific organic matter that has been degraded to lead and calcium oxalates is found in younger glazed pieces subjected to an atmospheric environment.

1. Introduction

Lead and tin-glazes have been widely produced since antiquity for decorating tiles and earthenware pottery due to their ability for improving the utilitarian qualities of ceramic objects by making them impervious to liquids and providing a bright and colored appearance. First known production of lead-glazed pottery comes back to the first century BC in Anatolia and becomes common in the Roman period and, after this, in Europe and Near East throughout the Middle Ages [1,2]. Use of raw materials containing Pb (II) such as litharge (PbO) or white lead ($2PbCO_3 \cdot Pb(OH)_2$) as fluxing agent provides smooth and clear glazes with superior properties that adhere well to the surface of the pre-fired pottery body. Additionally, lead-glazes interact properly with most metal oxides used to provide color (i.e. titanium, vanadium, chromium, manganese, iron, cobalt, nickel, or copper).

From the seventh to ninth centuries BC starts the production of low-temperature glazes opacified with lead stannate to yield yellow opaque glazes in Egypt and Syria [3] and glazes opacified with tin oxide by Islamic potters from Abbasid Iraq in an effort for imitating the Chinese porcelain that requires a high-temperature firing [4]. This manufacturing technique was progressively transmitted eastwards to Syria and Iran and westwards to Europe from Northern Africa and the Iberian Peninsula [5,6].

The chemical composition of lead and tin-glazes was varying over time. First glazes were prepared as alkali glazes with a PbO low content of 1-2 %. The lead content was progressively increased to that of a lead-alkali glaze (20-40 % PbO and 5-12 % alkali) achieving a value of 55 % PbO and 3 % alkali in Hispano-Moresque pottery [1].

The first Hispano-Moresque lead-glazed ceramics dated in the Iberian Peninsula were found in workshops located in the southeast of al-Andalus, (at ca. 850–875 AD) [7]. This first decorated pottery exhibited a transparent lead-glaze green and/or honey-colored by using copper and manganese as chromophore elements. First lead-glazes using tin as opacifier were found in al-Andalus in the ninth century BC [8]. Decorations with metal oxides were developed in the Iberian Peninsula since the tenth century, starting with green (copper) and brown (manganese) designs on a white tin glaze [9]. Blue and yellow decorations using metal oxides (cobalt as blue chromophore) and (antimony forming lead antimonate grains as yellow chromophore) were also produced in Hispano-Moresque workshops together with lusterware (three-firing processes) associated with blue decoration [10]. In particular, tin-glazed earthenware (green and brown, blue and white, and luster) was produced in Valencian workshops of Paterna, Manises, Valencia, and Xàbia (Spain) [11-14], and were widely exported in the thirteenth and fourteenth centuries [15]. These typologies [16] and new polychrome typologies were successively developed in further centuries in Europe [6,12,17-19].

Concerning studies of alteration processes, abundant literature is found describing alteration mechanisms of glass [20-23] and, more specifically, those that take place in

museum environments [24,25], historic stained glass used for decorating windows in churches and cathedrals [26-29], buried glass [30,31] and underwater glass [32-34]. Nevertheless, lesser works devoted to the study of the alteration processes of ceramic glazes are found in the literature [35]. In a study of the manufacturing technique of Roman sherds decorated with green lead-glazes De Benedetto et al. [36], identify a corrosion layer in the glaze but they do not provide the chemical composition of this corrosion layer. Salinas and Pradell [7] mention a lead leaching process accompanied by recrystallization of lead and calcium phosphates and carbonates inside surface cracks in lead transparent glazes made in al-Andalus (c. 875–929 AD), suggesting that these precipitation products act as cement for soil particles. Similarly, Molera et al. [10] found cerussite in an outer corrosion layer formed in buried manganese brown glazes from Murcia (Spain), dated back from the tenth century. Machado and Vilarigues [37] study the corrosion process of blue enamels on laboratory specimens that mimic old enamels used for decorating glass windows. According to eighteenth-century recipes, they prepare a base lead glass of alkali-lead type (37.6-43.2 % PbO, 12.3-17.9 % K_2O, 3.7-6.3 % Na_2O) and add smalt or zaffre (a mixture of SiO_2 and CoO (2:1, w/w)) as blue coloring agent. The analyses were performed by using inductively coupled plasma-atomic emission spectroscopy (ICP-AES), Fourier Transform Infrared Spectroscopy (FTIR), X-ray diffraction (XRD), and Fibre Optic Reflectance Spectroscopy (FORS), and confirmed that alkali ions are leached promoting a change of the chemical structure of the glaze matrix with the formation of Co^{2+}/Co^{3+} spinel crystals. Lixiviation of Pb^{2+} ions with recrystallization as cerussite and hydrocerussite in the surface was also described in this research. Yin et al. [38] study the corrosion processes of buried pieces of lead-based glazes from the Han dynasty (206 BC-220 AD). This analytical study used transmission and scanning electron microscopies (TEM, SEM), X-ray microanalysis (SEM-EDX), FTIR, and XRD. The study showed that the buried glazes underwent lead leaching that resulted in the formation of a lamellar Si-rich layer near the surface and an outer crystalline layer of precipitated lead carbonate. Zhou et al. [39] found underwater blue-and-white porcelain affected by devitrification, a process that resulted in a multi-layered outer structure. In prior papers, the authors of the present work described corrosion processes affecting buried glasses and tin-glazed ceramics using solid-state electrochemical techniques [40-43]. In agreement with these studies, lixiviation of alkaline and Pb^{2+} ions present in the glaze as network modifiers occurs significantly. This process results in the formation of a corrosion layer with lower lead content. In burial conditions, this migration is controlled by reactions of hydration, hydrolysis, and ion exchange in aqueous solution in a way similar to that described for buried glass [20-23], which results in the formation of a corrosion layer with a lamellar structure that macroscopically exhibits an iridescent appearance. It is known that lead-silicate glasses and glazes have a structure that combines network forming Pb^{4+} present as [PbO_4] tetrahedral unities together with Pb^{2+} ions as network modifiers with octahedral coordination [PbO_6] [44,45].

The preparation of cross-sections by the conventional metallographic procedure of embedding the sample in a curing resin and further polishing with abrasive disks and dispersions is a method abundantly used in the study of archaeological glazes and porcelains. The examination and analyses of the samples are carried out using optical microscopy (OM) in combination with SEM-EDX, field emission scanning electron microscope with an energy dispersive X-ray detector (FESEM-EDX), electron

microprobe analysis (EMPA), micro X-ray fluorescence, (μ-XRF), synchrotron-X-ray absorption spectroscopy (XAS), X-ray diffraction (XRD), or Raman spectroscopy, [46-51]. Focused ion beam (FIB) is a novel technique that is being increasingly used as a preparation method of ultra-polished cross-sections and lamella for the investigation of microstructure and phase transformation of materials related to ceramics using electron backscattered diffraction (EBSD) [52], and transmission electron microscopy (TEM) [53], respectively. Nevertheless, FIB, as a preparative technique, has been scarcely used for studying glazed ceramics. In the archaeometry field, FIB coupled with FESEM images was applied for the study of manufacturing technology of ancient lusterware ceramics with nanoparticle distribution in the outer glaze [54,55]. This work presents a study in which the novel technique of FIB is coupled to a FESEM-EDX (FIB-FESEM-EDX) for performing surface analysis at nanoscale. This new technique has been combined with classical OM and the advantages of FTIR spectroscopy for providing the molecular composition in the study of the surface corrosion exhibited by archaeological ceramics that have remained for centuries in different environments. To the knowledge of the authors, corrosion processes occurring in ceramic glazes have not still been studied utilizing FIB-FESEM-EDX. In prior works, the authors have successfully applied FIB-FESEM-EDX for studying both compositional and morphological corrosion processes occurring in the surface of copper-based coins [56,57]. Here, the proposed multi-technique approach has enabled the identification of corrosion processes on the surface of tin-glazes that morphologically only are appreciable at the nanoscopic scale. The dependence of corrosion processes on environmental conditions, glaze composition, and coloring agents behavior have also been discussed.

2. Material and methods

2.1. Description of archaeological pieces

Three glazed ceramic pieces that exhibited alteration processes have been selected taking into consideration the influence of the environmental conditions to which the pieces were subjected during centuries. A summary of the glazed ceramic characteristics and samples analyzed are presented in Table 1. Images of the ceramic pieces are shown in Fig 1.

2.2. Instrumentation

Microphotographs of the surface of glaze samples and samples prepared as cross-sections were acquired employing a Leica M165 stereo microscope using a capture system of high-resolution digital image IC80HD controlled by LAS software.

The glaze samples were analyzed with a FIB-FESEM Zeiss (Orsay Physics Kleindiek Oxford Instruments) model Auriga compact equipment. The operating conditions were: 30 kV, and current intensities of 500 μA, and 20 nA in the FIB for generating the focused beam of Ga ions that enabled the sectioning of samples and formation of trenches. The Ga beam impacts perpendicularly to the plane of the vertical wall of the trench by tilting 54° the stage where is placed the ceramic microsample. Secondary electron images were

acquired at 2 kV in the FESEM. Spot and area analyses were performed in cross-sections and trenches operating with an Oxford-X Max X-ray microanalysis system coupled to the FESEM controlled by Aztec software. A voltage of 20 kV and a working distance of 6-7 mm was used. ZAF method for semiquantitative microanalysis was applied. The counting time for acquiring X-ray spectra was 100 s. A more detailed description of the working conditions can be found as supplementary electronic material.

Due to the heterogeneity of the glazes at the microscopic scale, a minimum of three measurements were performed on the cross-sections in areas at ca (100x100 μm) for obtaining the average composition of the uncorroded glazes containing grains of unmelted pigment, raw materials, and neoformed phases dispersed in the vitreous matrix. Spot acquisition of X-ray spectra was also applied in both cross-sections and trenches for obtaining the average values of the chemical composition of the corroded and uncorroded vitreous matrix of glaze, grains of raw materials, pigments, opacifiers, and mineral phases neoformed during the firing process. X-ray spectra were acquired in spot mode on three different points of the glaze vitreous matrix or in different grains of the same mineral.

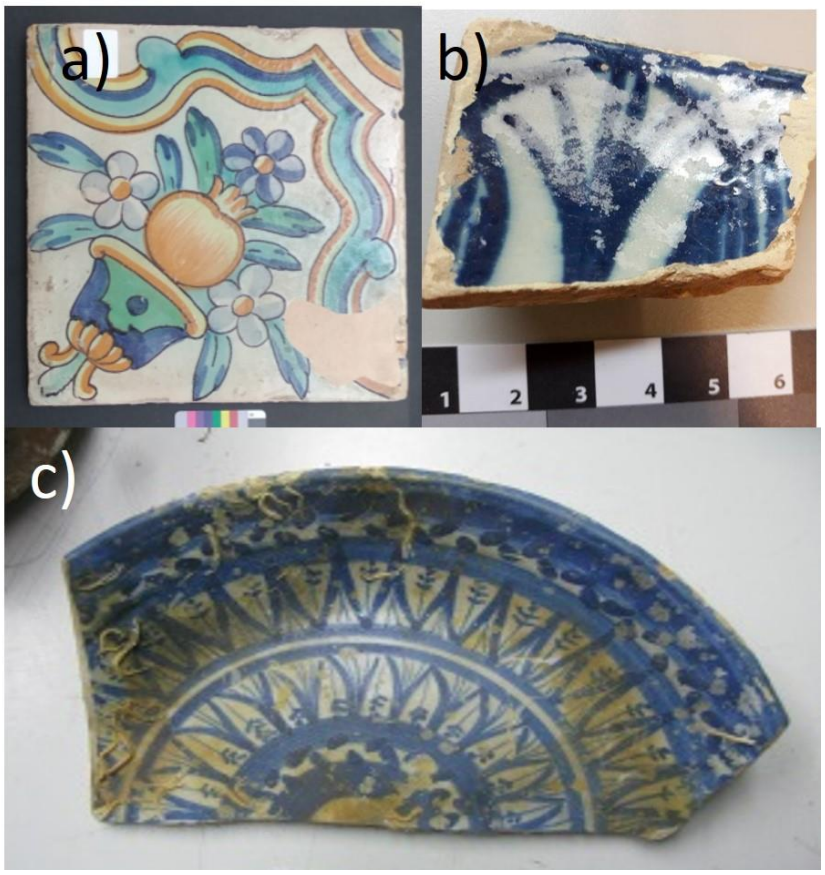

Figure 1.- a) Polychromed tin-glazed tile *A* (Valencia workshop, 18th century); b) fragment of blue and white tin-glazed dish *B* (Manises workshop, 15th century); c) fragment of blue and white tin-glazed dish *C* (Xàbia workshop, 19th century).

Table 1.- Description of studied pieces of glazed ceramic.

Object Reference	**Provenance**	**Chronology**	**Current location**	**Typology**	**Conservation state**	**Environmental conditions of the archaeological site**	**Sample reference**
A	Valencia workshop	18th century	Private collection (Valencia, Spain)	Polychromed tin-glazed tile	Smooth glaze with small pits randomly spread	Atmospheric	*A-1* (white), *A-2* (yellow), *A-3* (orange), *A-4* (brown), *A-5* (blue), *A-6* green)
B	Manises workshop	15th century	Stored in the Museu de Cerámica de Manises (Valencia, Spain)	Fragment of blue and white tin-glazed earthware	Large areas with iridescent corrosion	Burial	*B-1* (white), *B-2* (blue)
C	Xàbia workshop	19th century	Stored in the Museu Arqueologic i Etnografic de Xàbia (Valencia, Spain)	Dish of blue and white tin-glazed earthware	Lossed brightness	Submarine	*C-1* (white), *C-2* (blue)

FTIR reflection measurements were conducted on microsamples scraped from the ceramic glazes. IR absorption spectra were obtained in the attenuated total reflectance (ATR) mode using a Vertex 70 Fourier-transform infrared spectrometer with an FR-DTGS (fast recovery deuterated triglycine sulfate) temperature-stabilized coated detector and an MKII Golden Gate Attenuated Total Reflectance (ATR) accessory. The ATR-IR module has a diamond crystal with a refractive index of 2.4. The penetration depth of the probe is estimated to be about 600 nm at 3450 cm^{-1}, about 900 nm at 1650 cm^{-1} and about 600~630 nm in the 1030-1100 cm^{-1} region [58,59]. This probe depth is defined as the depth at which the IR beam intensity is attenuated by ($1-e^{-1}$) [60]. 32 scans were collected at a resolution of 4 cm^{-1} and the spectra acquired were processed with OPUS/IR 7.2 software. Deconvolution and curve-fitting analysis were applied to the IR overlapped bands of silicate group in the range 1260-600 cm^{-1}. The methodology applied has been described elsewhere [61].

2.3. Preparation of samples for the analyses

The chemical analyses of this study were carried out on microsamples (surface area lesser than 1 mm^2) excised from the glaze of the ceramic pieces using scalpels. Sampling points were selected with the help of an optical microscope to avoid areas with fissures, cracks, and other superficial irregularities in all the glazed pieces and earth deposits in the burial fragments. Additionally, microscopy examination enabled better discrimination of the different colored areas in each glaze.

The microsamples excised from the glazes were prepared in three different modes:

A) Microphotographs with OM and electron images and X-ray spectra using FESEM-EDX were acquired on cross-sections prepared using polyester resin (Glasspol 328, Glasspol Composites SL, Spain), which does not require heating for curing, followed by polishing with SiC dishes of decreasing grain size. This preparation technique allowed the analysis of the entire cross-section of the glaze.

B) Electron images and X-ray spectra were also acquired on trenches formed using the FIB on microsamples excised from the glazes. The microsamples were fixed with carbon adhesive to the aluminum stage of the FESEM. The size of trenches was (10x8 μm). Points for performing the trenches in the glaze microsamples, whose surface exhibited a homogeneous appearance, were chosen avoiding areas where cracks, pits, fissures, or mineral microdeposits were present.

Both microsamples and cross-sections were carbon-coated before the analysis by FIB-FESEM-EDX and FESEM-EDX, respectively. In the microsamples where trenches were performed, a second treatment before the formation of the trench was carried out that consisted of applying a thin layer of Pt on the area where the trench should be performed

to protect the surface of the glaze at the nanoscale from possible alterations due to the Ga ions bombardment during the formation of the trench.

C) The third series of microsamples of glazes were analyzed by FTIR spectroscopy in ATR mode. IR spectra of the outer corrosion layer in the aerial and buried glazes and the uncorroded submarine glaze were directly acquired on the surface of the microsamples. The IR spectrum of the amorphous inner corrosion layer of the buried glaze was acquired by mechanically removing the fragile outer lamellar layer whereas the IR absorption spectrum of the uncorroded buried glaze was acquired by powdering the microsample after mechanically removing the corrosion layers.

3. Results and discussion

3.1 Surface analysis with FIB-FESEM-EDX

3.1.1. Atmospheric environment

Microsamples excised from six areas in tile *A*, which represent the white glaze and the main colors used by the craftsman, were analyzed. At the naked eye, the surface of the tile had a glassy shine denoting an apparent absence of corrosion processes. Nevertheless, a microscopy examination of the tile at low magnification showed fissures, in particular, in orange areas, and pits randomly distributed on the surface. The pigment was densely spread in the motifs decorated in orange and brown whereas white opaque crystalline aggregates dispersed into the translucent glassy matrix appeared in the white, yellow, green, and blue areas. Yellow aggregates were also identified in the yellow and green motifs of the decoration. In green and blue motifs, the glassy matrix was homogeneously died (see Fig. 1S provided as supplementary electronic material). The thickness of the glazes ranges between 180 μm in the green sample to 260 μm in the yellow sample. Microphotograph and backscattered electron image of the cross-section and secondary electron images of the orange microsample and the trench formed on its surface are shown in Fig. 2. The micromorphology observed is in agreement with that reported for ceramic glazes of the seventeenth and eighteenth centuries. As can be seen in the images (Fig 2a,b), the glaze exhibits some bubbles of different sizes. Small grains of tin oxide, the opacifier used, are heterogeneously distributed and, eventually, form small clusters some of which are located in the inner surface of the bubbles [62]. Raw materials remnants appear randomly distributed along the glaze as coarse grains (2-30 μm) of quartz ($SiO_{1.79}$) and potassium feldspar ($K_{1,0}Al_{1,0(0,1)}Si_{3,0(0,2)}O_8$) (Fig. 2a,b). Undissolved grains of pigment with various sizes ranging between 10 to 1 μm or less are concentrated in the subsurface of the glaze forming a layer of over 40 μm thickness. That confirmed the use of the in-glaze decoration technique characterized by the application of the pigment on the surface of the glaze before the second firing (Fig. 2a,b). X-ray analyses performed in the pigment grains confirmed that the orange motifs are the result of using Naples yellow pigment ($Pb_{2,00}Sb_{2,03(0,02)}O_7$) (*vide infra* FTIR analyses) with added Fe_2O_3 for obtaining

more reddish hues [10,62]. Scarce neoformed grains are present in the interphase of the glaze and the ceramic body, which confirms a low interaction of both as a result of the double firing process [1,11].

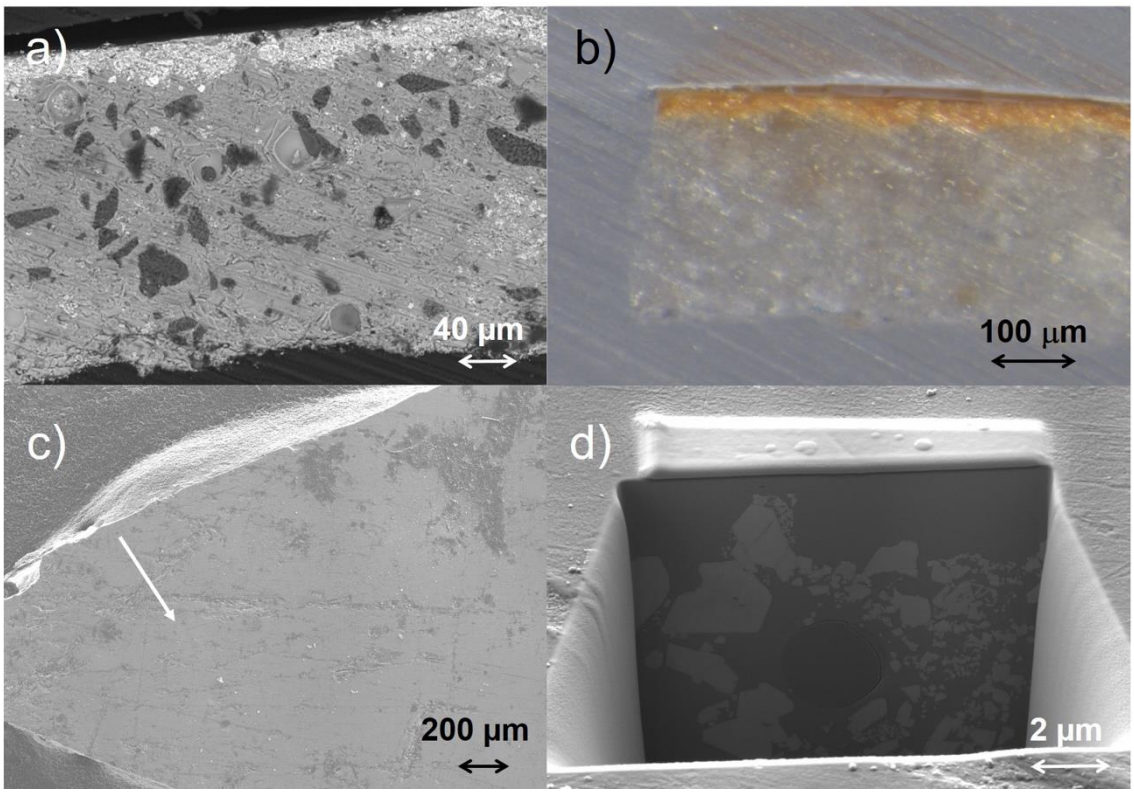

Figure 2.- Zone orange (*A*-3) of the polychromed tile *A*: a) Backscattered electron image of the cross-section; b) microphotograph of the cross-section (PPL); c) secondary electron image of the surface of the sample in the zone where the trench was performed (position of the trench is pointed out by an arrow); d) secondary electron image of the trench formed in the surface of the orange glaze.

Fig. 3 shows in detail the outer part of the FIB trenches formed in the six microsamples taken from the different colored areas of the tile. A thin corrosion layer is observed on the surface of all glazes. Brown and blue glazes (Figs. 3a,e) show the thickest corrosion layers with an irregular thickness (30-500 nm). Some pore and infiltration channels 1.3-2 µm deep are also observed for which, presumably, the corrosion process advances towards the glaze core. The corrosion layer appears as broad isolated spots on the surface of the green glaze (fig. 3d). Glazes orange, yellow, and white (Fig. 3b,c,f) exhibit a thinner corrosion layer that achieves a thickness of 25 nm in the orange sample. A few nanometric cassiterite crystals and pores are recognized in the corrosion layer of these glazes. The formation of fine cassiterite crystals has been well described previously based on a dissolution process of the PbO-SnO_2 mixture to form the metastable compound $PbSnO_2$ that transforms in small crystals of SnO_2 with dimensions lower than 1 µm during cooling [63]. Bigger grains of tin oxide with angular forms were found in the glaze, which could

have been associated with raw material remnants after the grinding process of the fritted product obtained by heating lead and tin metals [14]. The corrosion layer is surrounding a big grain of Naples yellow in the yellow glaze (Fig. 3c). It can also be seen abundant subangular grains of lead antimonate with variable sizes under 2 µm mixed with small grains of cassiterite in the subsurface of the orange glaze (Fig. 2d). The dark rounded grain in the center of this trench exhibited a chemical composition rich in Fe and K that has been ascribed to raw materials providing this element according to Piccolpasso's treatise. In this manuscript is described that orange colors were prepared with mixtures of lead oxide, antimony oxide, and wine lees, with iron scale (i.e., iron oxide), for obtaining the suitable orange color in combination with Naples yellow [6].

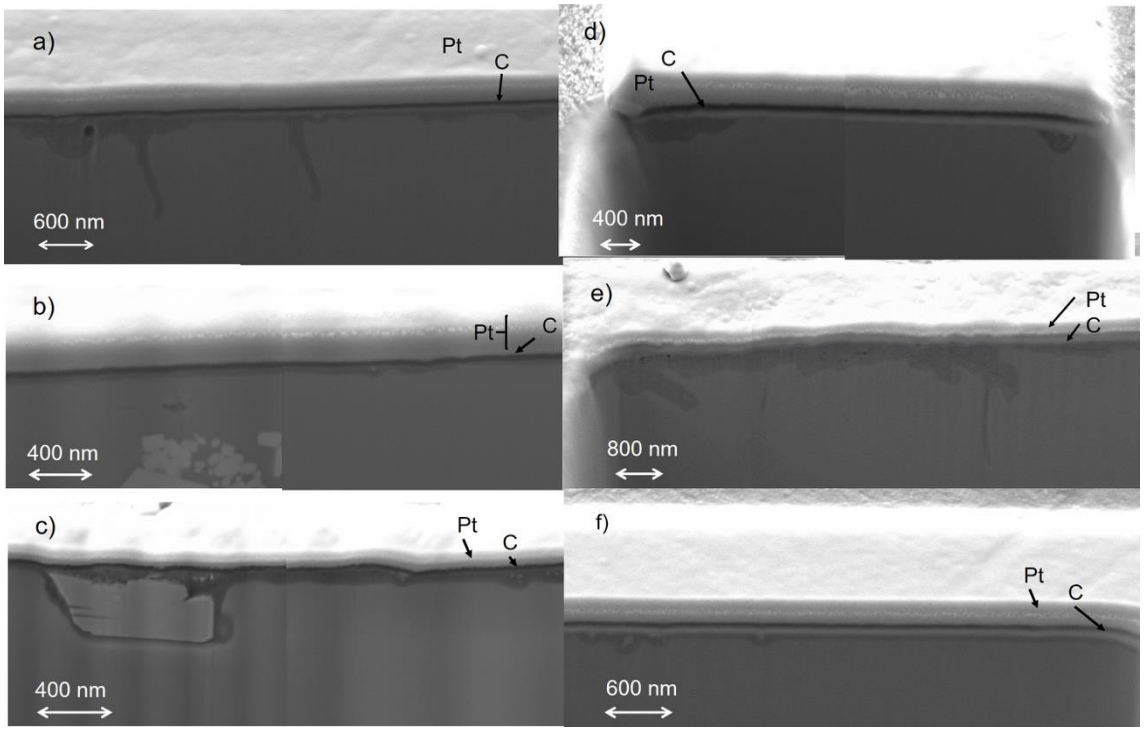

Figure 3.- Secondary electron image (2 kV) of the outer part of the trenches performed in the different colored areas of the surface of the glaze of tile *A*. Detail of the thin corrosion layer formed in the glaze can be seen in all the trenches: a) brown; b) orange; c) yellow; d) green; e) blue; f) white.

Table 2 summarizes the average composition of the uncorroded bulk of the glaze obtained in the cross-section of the white glaze using FESEM-EDX. According to the classification established by Tite et al. [1], this glaze can be considered a lead alkali glaze with a 21 % PbO and total alumina, alkali, and alkaline earth oxides content of 16.5 %. This composition is in agreement with those reported for maiolica tin glazes manufactured in other production centers of Spain and Europe during the seventeenth and eighteenth centuries [18,62-65]. Nevertheless, it should be noted the comparatively high potash content of 10.6 % is associated with the feldspar-rich sand used as raw material highlighted by the abundant unmelted grains observed in the cross-section. These results suggest that this tile was prepared according to the traditional technique in which a

mixture of lead and tin is calcined to produce a powdered material named *calx*. After this, silica and an alkaline frit are added to the *calx* and then again heated [67]. The 3.4 PbO/SnO and 2.6 [glaze/(PbO+SnO)] ratios found in the *A* glaze are within the ranges 2.8-6-9 and 0.7-2.7 established by Tite et al. [66] for tin-lead *calx*. On the other hand, the SnO content of 6.2 % is in the range of 5-10 % SnO established by Molera et al. [10] for providing the suitable opacity to the glaze.

Concerning the pigments, the X-ray microanalysis carried out on the different areas has confirmed the use of Naples yellow for yellow, Naples yellow, and iron from wine lees and iron scale for orange and manganese oxides as coloring agents for brown. X-ray analyses performed on outer areas of the *A*-5 blue cross-section show Co accompanied by As suggesting that zaffre was used as raw material for blue motifs. It has been reported that zaffre, a cobalt oxide by-product of the silver mining industry, which is prepared by roasting cobaltite (CoAsS) and erythrite ($Co_3(AsO_4)_2 \cdot 8H_2O$), was commonly used as blue pigments in Europe between the sixteenth to eighteenth centuries [6]. The mixture of particles of lead antimonate and the copper diluted in the glaze agrees with the mixed copper green color described in Piccolpasso's treatise that consists of a prefired mixture of copper oxide with lead oxide and antimony oxide [6]. It is interesting to note that copper is identified not only in green areas but also in white and brown areas. This unexpected finding is associated with the great diffusivity of this ion in the melted glaze beyond the profile of the green areas [68].

As it is shown in Table 2, X-ray spectra acquired in the trenches, in both corrosion layer and uncorroded inner glaze, confirmed that silica content increases in the corrosion layer. A low shift in the content values of network modifier ions is also found, however, different behaviors are observed depending on the ion. Potassium and magnesium content slightly diminish, which confirms the diffusion of these network modifiers from the uncorroded glaze. Nevertheless, a higher content is found for lead and calcium in the corrosion layer, which suggests that precipitation processes are taking place that retain these network modifier ions in the open network of the corrosion layer. These results can be interpreted in light of general models of glass corrosion. Environmental humidity generates water microdrops that attack the glaze and result in ion exchange of network modifiers. In particular, the ion exchange of the Pb^{2+}network modifier ions goes by the process:

$$2(Si–O)–Pb + 2H^+ \rightarrow 2(Si–OH) + Pb^{2+} \quad (1)$$

In parallel, hydrolysis of the silicate groups takes place forming silanol groups that distort and progressively open the structure of the network with the concomitant loss of cohesion. These processes result in a modification of the pH of the attacker solution [21]. The most open and porous silica-rich gel layer formed favors the infiltration of external ions and the reaction of atmospheric carbon dioxide with the dissolved ions forming insoluble carbonates and bicarbonates of calcium and lead, that remain retained in the porous

structure of the gel layer. If this process is produced in abundance, an outer precipitation layer can be formed [37,69-71]. In parallel, the metabolic action of microorganisms can promote the occurrence of oxalate salts [28,71,72]. The presence of carbonates, mainly, calcium and lead carbonates as well as calcium and lead oxalates in the corrosion layer of tile *A* has been confirmed by FTIR spectroscopy as described thereafter.

3.1.2. Burial environment

The iridescent aspect of the altered areas of the surface of fragment *B* is shown in Fig. 2S. Figures 4a-c and 3S show the backscattered electron images and photographs, respectively, of the cross-sections obtained in two samples taken from the white (*B*-1) (Fig. 4a and 3Sa) and blue (*B*-2) (Fig. 4b and 3Sb) areas of the fragment *B* (Manises workshop, 15th century) decorated with blue motifs on a white tin glaze. The white glaze has a thickness at ca. 90-120 μm. Although no bubbles are formed, abundant grains of unmelted Co-rich blue pigment are seen in the interphase with the ceramic body. This finding confirms that this piece was made by applying the pigment for drawing the motifs of blue decoration before covering the ceramic body with the tin glaze. This technique is the so-called "underglaze technique" [73,74]. The average values of oxide wt% of the glaze listed in table 3 are in agreement with data reported in prior studies for medieval lead alkali glazes from Valencian workshops [67]. It is remarkable the high tin content (11.7-7.4 % SnO) that reduces the PbO/SnO ratio until 3.2. A corrosion layer is recognized on the surface of both white and blue glazes. This layer, in turn, comprises two sub-layers (see arrows in Fig. 4S). The upper one (1 in Fig 4a,b) exhibits a lamellar structure whereas the inner one (2 in Fig. 4a,b) has an amorphous morphology. These corrosion sub-layers can be studied in more detail in the FIB trenches formed in both blue and white areas, which are shown in Figs. 5 and 6. The lamellar sub-layer (Fig. 5b,d, and 6b,d) has a minimum thickness in the range 20-30 μm whereas the thinner amorphous sub-layer (Fig. 5a,c and 6a,c) has a thickness ranging between 1600-340 nm. It is interesting to note that the abundant presence of nanopores formed on the lamella (Fig. 6b,d) as well as on the top of the amorphous sublayer (Fig 6c) could be observed uniquely in the trenches due to the finest polishing of the cross-section achieved with FIB technique. The images obtained confirm that this ceramic glaze has undergone a corrosion mechanism according to that described previously for buried lead glasses [38,69,70,75-77]. The seasonal humidity-dryness cycles in the soil promote, in a first step, an enrichment in silica of the corrosion layer. Progressively the corrosion layer acquires abundant porosity that, concomitantly, promotes the penetration of the attacker solution containing exogenous ions such as H^+ and CO_3^{2-}. The H^+ ions favor the advance of the hydrolysis reaction.

The leached Pb^{2+} ions can combine with CO_3^{2-} ions and precipitate forming lead carbonate that remains infiltrated in the lamellar layer and, in extreme instances, forms an outer precipitation layer of cerussite and hydrocerussite. During the dryness step the processes pass slowly forming an interlaminar space of a few hundred nanometers and

the sequence starts again with the new humidity step in which the attacker solution penetrates forming a new lamella.

Average chemical compositions obtained on the uncorroded glazes as well as on the amorphous and lamellar corrosion layers of samples *B*-1 and *B*-2, using the FESEM-EDX, are listed in table 3. The more remarkable changes are the progressive increase of the silica and tin oxide content from the uncorroded glaze to the amorphous and lamellar sublayers. The former indicates that ion exchange and hydrolysis reactions have taken place extensively. The increase of the tin oxide content is due to the high insolubility of the cassiterite microcrystals that remain trapped in the corrosion layers. In parallel to these changes, a notable decrease in the content of lead oxide is found from the uncorroded to the corroded layers. That suggests that most of the lead present as mobile Pb^{2+} network modifier ion has migrated outside. The fraction of lead that remains in the corroded layers is supposed to be present as Pb^{4+} network former and as lead carbonate insoluble salts formed by the precipitation of Pb^{2+} ions with exogenous carbonate ions in the more open Si-enriched network of the corrosion sublayers. A low decrease of content is also observed in the rest of the elements from the uncorroded glaze to the outer lamellar sublayer with a slight increase in the latter sublayer in some of them. This result suggests that most of these mobile ions have been lixiviated with partial precipitation to insoluble salts in the outer sublayer.

Table 2.- Chemical compositions measured in the cross-section of the white area of tile (*A*-1) and the trenches formed in samples of the different colors of tile *A* using FIB-FESEM-EDX. Standard deviation in brackets.

Component	Cross-section	Chemical composition (% oxide)											
		Trench											
	A-1	A-1		A-2		A-3		A-4		A-5		A-6	
	Glaze*	G.M.	C.L.	G.M.	C.L.	G.M.	C.L.	G.M.	C.L.	G.M.	C.L.	G.M.	C.L.
Na_2O	0.4(0.1)	n.d.	0.30(0.01)	n.d.	0.4(0.1)	n.d.	n.d.	n.d.	n.d.	n.d.	1.0(0.1)	n.d.	0.5(0.3)
MgO	0.5(0.1)	n.d.	0.41(0.03)	n.d	n.d.	0.4(0.1)	0.7(0.1)	n.d.	n.d.	n.d.	0.3(0.1)	n.d.	0.46(0.03)
Al_2O_3	2.7(0.2)	1.4(0.1)	0.97(0.2)	1.1(0.1)	0.9(0.1)	1.3(0.2)	1.6(0.1)	1.1(0.1)	1.0(0.1)	1.3(0.1)	1.0(0.1)	1.46(0.03)	1.4(0.1)
SiO_2	55.1(0.9)	51.6(0.5)	52.3(0.4)	51(0.4)	52(0.3)	44(1)	48(1)	53(1)	58(1)	61(1)	62(1)	52.2(0.7)	54.4(0.4)
Cl	n.d.	n.d.	n.d.	n.d.	n.d.	n.d.	n.d.	n.d.	n.d.	n.d.	0.3(0.1)	n.d.	n.d.
K_2O	10.6(1)	13.8(0.2)	10.9(0.3)	9.3(0.03)	9.6(0.02)	9.3(0.2)	8.7(0.1)	10.4(0.1)	7.9(0.3)	10.7(0.1)	9.8(0.2)	13.2(0.6)	10.7(0.4)
CaO	2.7(0.5)	3.4(0.3)	3.7(0.3)	2.2(0.1)	2.7(0.1)	4.4(0.2)	3.9(0.1)	3.0(0.2)	3.5(0.3)	2.8(0.1)	3.2(0.1)	3.1(0.1)	3.2(0.3)
MnO	n.d.	n.d.	n.d.	n.d.	n.d.	n.d.	n.d.	0.5(0.1)	n.d.	n.d.	n.d.	n.d.	n.d.
FeO	n.d.	n.d.	n.d.	n.d.	n.d.	4.5(0.1)	3.6(0.1)	0.5(0.1)	n.d.	0.3(0.1)	0.4(0.1)	n.d.	0.1(0.3)
CoO	n.d.	n.d.	n.d.	n.d.	n.d.	n.d.	n.d.	n.d.	n.d.	1.1(0.1)	n.d.	n.d.	n.d.
As_2O_3	n.d.	n.d.	n.d.	n.d.	n.d.	n.d.	n.d.	n.d.	n.d.	0.03(0.1)	n.d.	n.d.	n.d.
CuO	0.8(0.6)	n.d.	n.d.	n.d.	n.d.	0.8(0.1)	n.d.	1.0(0.1)	n.d.	n.d.	n.d.	2.6(0.2)	2.3(0.1)
SnO	6.2(1)	2.9(0.4)	2.5(0.8)	2.1(0.1)	1.7(0.1)	n.d.	n.d.	3.6(0.2)	n.d.	2.6(0.1)	1.7(0.1)	n.d.	n.d.
Sb_2O_3	n.d.	n.d.	n.d.	n.d.	n.d.	7.4(0.2)	4.3(0.1)	n.d.	n.d.	n.d.	n.d.	n.d.	n.d.
PbO	21(1)	27.0(0.4)	28.9(0.9)	34(1)	36(1)	28(1)	30(1)	27(1)	29(1)	20(1)	21(1)	25.1(0.4)	27.1(0.7)

G.M.: glassy matrix of the glaze; C.L.: corrosion layer; n.d.: non detected; * Average composition measured in the cross-section

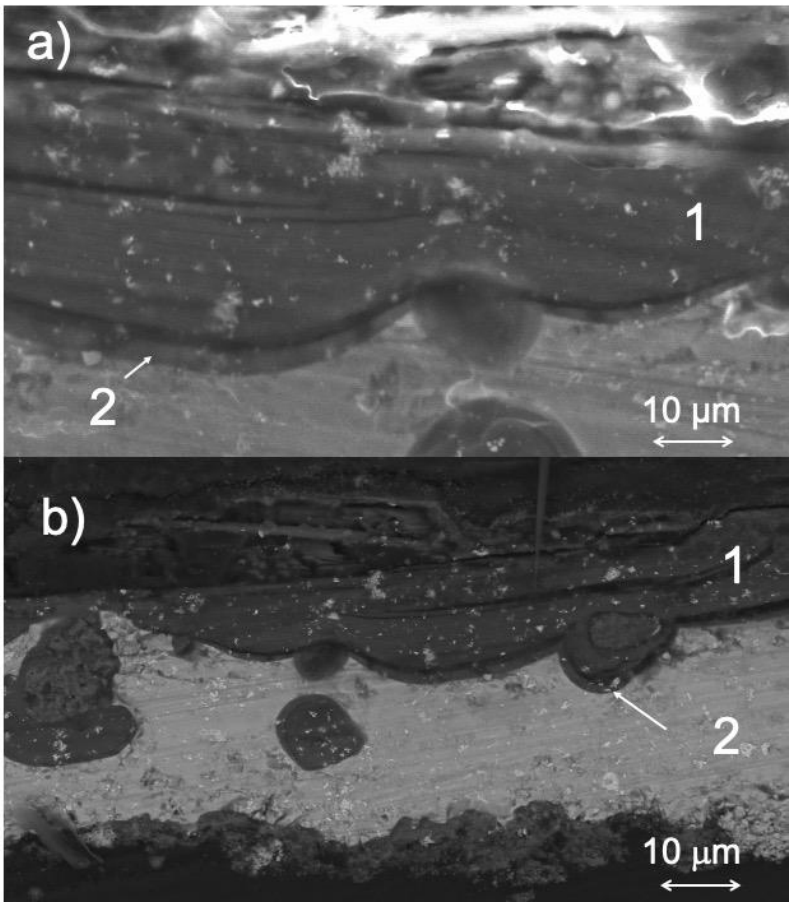

Figure 4.- Backscattered electron images (2 kV) of the cross-section of blue and white samples from ceramic fragment *B* (Manises workshop, 15th century). A) *B*-1 white glace (1: outer lamellar corrosion layer; 2: inner amorphous gel layer); B) *B*-2 blue glaze (1: outer lamellar corrosion layer; 2: inner amorphous gel layer).

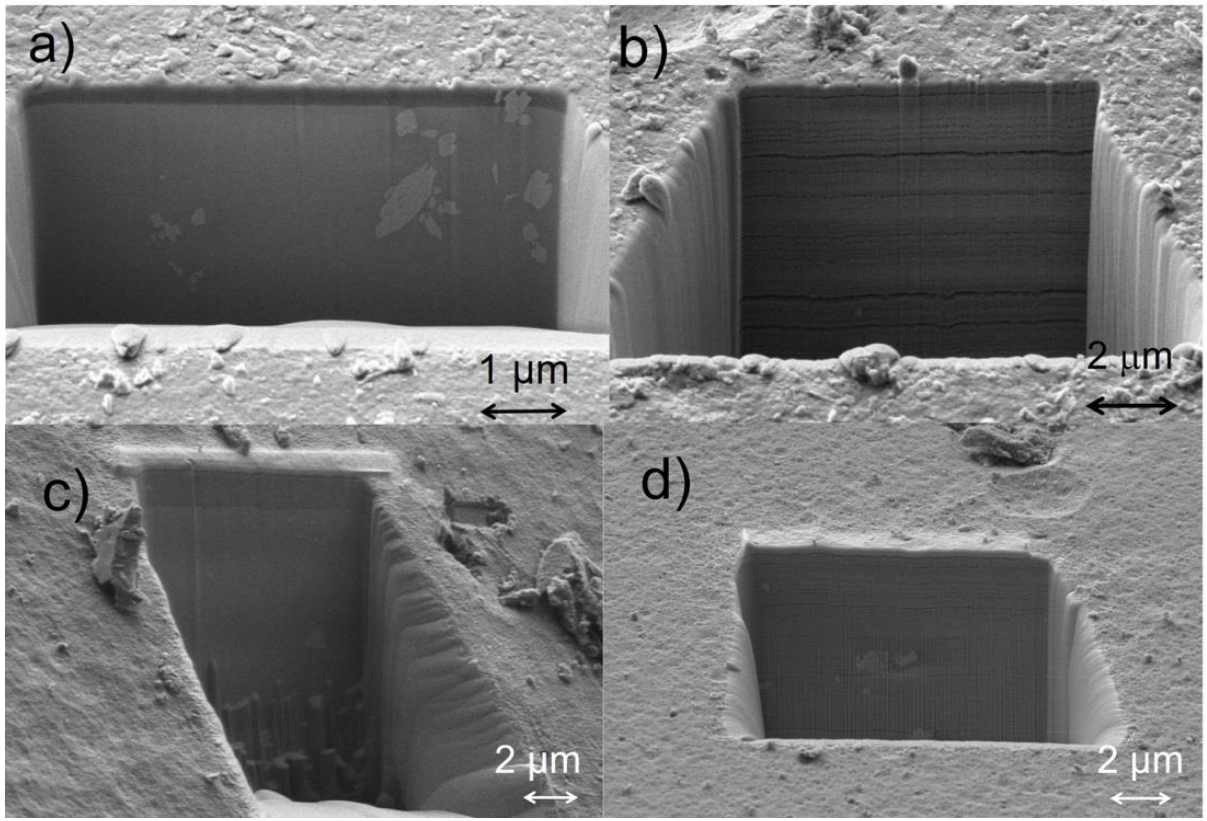

Figure 5.- Secondary electron image (2 kV) of the trenches performed in the colored areas of the glaze of fragment *B*: a) area of blue glaze *B*-2 with an amorphous layer of corrosion; b) area of blue glaze *B*-2 with an outer lamellar layer of corrosion; c) area of white glaze *B*-1 with an amorphous layer of corrosion; d) area of white glaze *B*-1 with an outer lamellar layer of corrosion.

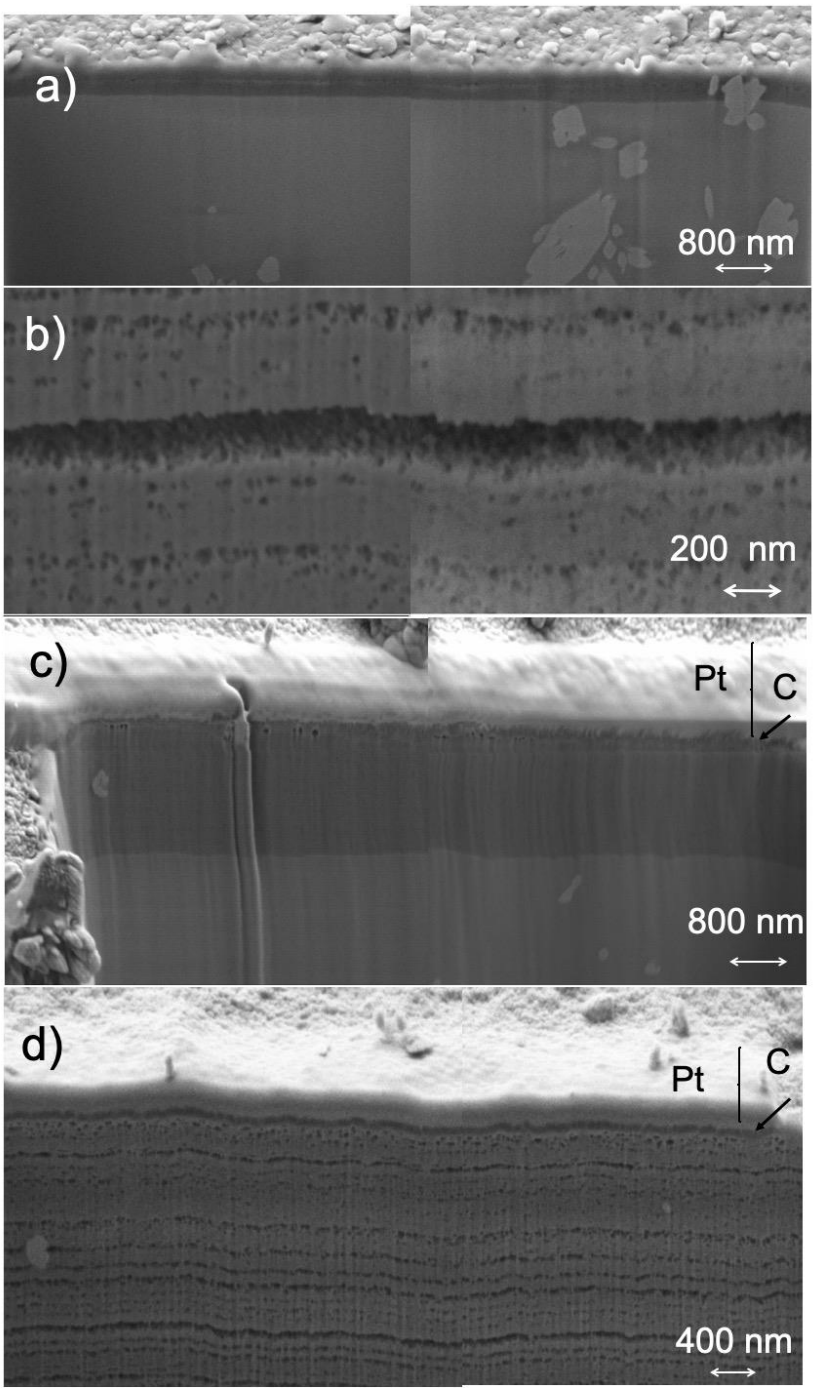

Figure 6.- Secondary electron image (2 kV) showing in detail the outer part of the trenches of figure 5: a) area of blue glaze *B*-2 with an amorphous layer of corrosion; b) area of blue glaze *B*-2 with an outer lamellar layer of corrosion; c) area of white glaze *B*-1 with an amorphous layer of corrosion; d) area of white glaze *B*-1 with an outer lamellar layer of corrosion.

Table 3.- Chemical compositions measured in the cross-section and the trenches formed in samples of the two colors of fragment *B* using FIB-FESEM-EDX. Standard deviation in brackets.

	Chemical composition (% oxide)							
	Cross-section		**Trench**					
Component	**Glaze***		**B-1 white**			**B-2 blue**		
	B-1	**B-2**	**G.M.**	**A.C.L.**	**L.C.L.**	**G.M.**	**A.C.L.**	**L.C.L.**
Na_2O	0.7(0.1)	0.6(0.1)	n.d.	n.d.	n.d.	0.3(0.3)	0.3(0.4).	0.6(0.1)
MgO	n.d.	n.d.	n.d.	n.d.	n.d.	n.d.	n.d.	0.2(0.4)
Al_2O_3	2.5(0.2)	2.1(0.2)	1.8(0.1)	5.2(0.1)	3.6(0.2)	2,0(0.1)	5.6(0.2)	5.7(0.5)
SiO_2	41(1)	40(1)	41(1)	56(1)	60(1)	43(1)	63(2)	66(3)
Cl	n.d.	n.d.	n.d.	n.d.	0.3(0.1)	n.d.	n.d.	n.d.
K_2O	6.0(0.3)	6.1(0.2)	10.9(0.3)	9.3(0.2)	8.7(0.1)	6.4(0.3)	5.3(0.3)	5.2(0.3)
CaO	2.2(0.2)	2.8(0.3)	4.1(0.2)	3.9(0.2)	2.7(0.2)	3.3(0.2)	2.4(0.3)	2.9(0.1)
FeO	n.d.	2.2(0.1)	3.9(0.2)	1.1(0.1)	1.5(0.1)	2.1(0.5)	3.0(0.2)	1.1(0.1)
CoO	n.d.	1.0(0.1)	n.d.	n.d.	n.d.	0.9(0.3)	n.d.	n.d.
SnO	11,4(0,5)	7.7(0.7)	5.9(0.1)	6.1(0.1)	18.4(0.1)	1,0(0.2)	5.0(0.4)	15(1)
PbO	36(1)	38(1)	35(1)	23(1)	8(1)	41(1)	16(1)	5(1)

G.M.: glassy matrix of the glaze; A.C.L.: amorphous gel layer of corrosion; L.C.L.: lamellar corrosion layer; n.d.: non detected; * Average composition measured in the cross-section.

3.1.3. Underwater environment

Dish *C* exhibited alterations notably different from those found in the two prior pieces examined. The observation with a light microscope showed in detail the significant erosion undergone by the glaze that looked micro rough surface Figure 5S. The cross-section examined by light microscopy (Fig. 6S) and FESEM (Fig. 7) was characterized by the abundant presence of bubbles and large grains of raw materials mainly quartz ($Si_{1,0(0,1)}O_2$) and K-feldspar ($K_{1,0(0,1)}\ Al_{1,1(0,1)}Si_{3,2(0,1)}O_8$). Cassiterite microparticles are randomly distributed in the glassy matrix often forming small clusters and cobalt pigment appears homogeneously diffused from the surface of the glaze. The thickness of the glazes is in the range of 235-560 µm. The average values of oxide wt% content of the glaze obtained in the cross-section (see table 4) are in good agreement with the composition of tin lead-alkali glazes according to the classification of Tite et al., [1]. This type of glaze is characterized by a PbO content below 35 oxide %. The high ratio PbO/SnO is associated with the abundance of unmelted grains of quartz and K-feldspars that contribute to the opacification of the glaze and then enable the reduction in the content of SnO. On the other hand, the value 2.0 found in the *C* glaze within the range 0.7-2.7 for the ratio [glaze/(PbO+SnO)] confirms the use of lead-tin *calx*.

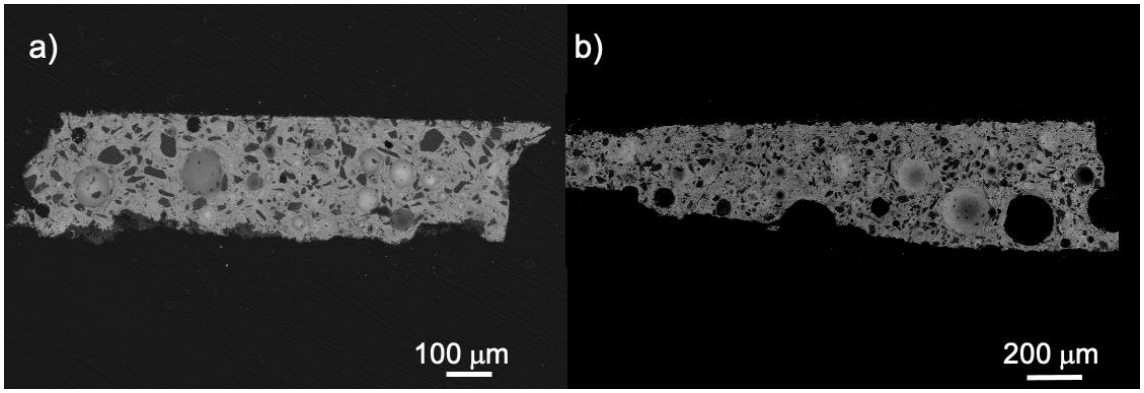

Figure 7.- Backscattered electron images (2 kV) of the cross-section of samples from the blue and white dish *C* (Xàbia workshop, 19th century). A) *C*-1 white glace; b) *C*-2 blue glaze.

Figure 8 shows the trenches formed on samples of white (*C*-1) and blue (*C*-2) glaze areas of the dish. Average values of the chemical composition obtained in the trenches are listed in table 4. The values of silica and alumina in the glassy matrix exposed in the trenches are lower than those found in the bulk glaze average composition from the cross-section. This result is associated with the abundant quartz and K-feldspar grains that contribute to increment the SiO_2 and Al_2O_3 content in the average composition of the bulk glaze in the cross-section.

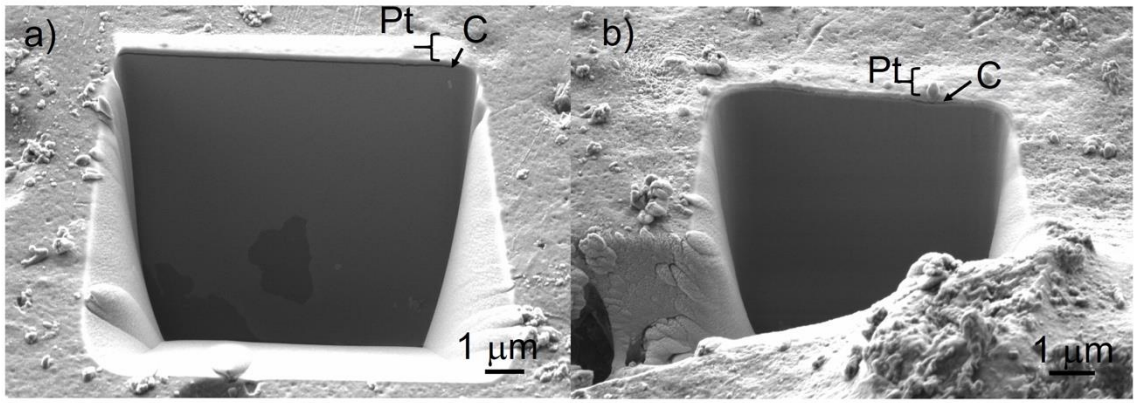

Figure 8.- Secondary electron images (2 kV) of the trenches formed in samples of dish *C*: a) area of white glaze *C*-1; b) area of blue glaze *C*-2.

Table 4.- Chemical compositions measured in the cross-section and the trenches formed in samples of the two colors of the fragment *C* using FIB-FESEM-EDX. Standard deviation in brackets.

Component	Chemical composition (% oxide)			
	Cross-section		Trench	
	Glaze*		C-1 white	C-2 blue
	C-1	C-2	G.M.	G.M.
Al_2O_3	3.9(0.2)	3.7(0.2)	2.98(0.2)	2.1(0.2)
SiO_2	55(1)	53(1)	51.3(0.2)	49.7(0.2)
K_2O	5.8(0.2)	5.7(0.2)	5.9(0.2)	6.2(0.2)
CaO	2.0(0.3)	1.3(0.3)	n.d.	2.7(0.1)
CoO	n.d.	0.2(0.1)	n.d.	0,13(0.05)
SnO	2.0(0,3)	4.4(0.3)	2.1(0.1)	0.3(0.1)
PbO	31(1)	31(1)	36(1)	38(1)

G.M.: glassy matrix of the glaze; n.d.: non detected; * Average composition measured in the cross-section.

From a morphological point of view, it is remarkable the absence of corrosion layer in the glaze surface, that makes a difference between the behavior of tin glazes exposed to marine and those others in burial or atmospheric environments. The absence of a corrosion layer can be interpreted in the light of the high ability of the seawater for dissolving the Si-network. The general models for deterioration of glass and glazes in contact with aqueous solutions establish that the attack of the aqueous solution results in the hydrolytic breaking of the ≡Si–O–Si ≡ superficial network groups according to the reaction [21]:

$$\equiv Si–O–Si \equiv + H^+ + OH^- \rightarrow \equiv Si–OH + HO–Si \equiv + H^+ \qquad (2)$$

In parallel, another mechanism starts, which results in the ion exchange of network modifiers, mainly Pb^{2+} and K^+ in the case of the studied tin glazes of the lead potash-rich type, according to the reaction (1). These processes promote the progressive destruction of the network and the formation of soluble silicic acid ($Si(OH)_4$) [21]. In marine solutions with high ionic strength, like that of the Mediterranean sea, the silicic acid molecules remain isolated or form small aggregates so that they can be assimilated by some aquatic microorganisms such as diatoms. This hypothesis is sustained by the secondary electron images obtained on the surface of the glazes. Figs. 9a,b show abundant unmelted grains of raw materials (quartz and K-feldspar) that are protruding the glassy matrix due to their higher resistance to chemical and microbiological marine deteriorating agents. Concave sockets and broad fissures filled with abundant microcrystals as well as linear and curved marks are associated with microorganisms' activity. The latter can be better understood in Figs. 9c,d where are identified microorganisms of navicular diatom type, of fusiform

morphology (Fig. 9c), and other globular algae (Fig. 9d). It is interesting to note that the diatoms are located in the sinus of the concave sockets. These cavities have probably been the result of the metabolic activity by which these microorganisms obtain the silicon necessary for forming their shells.

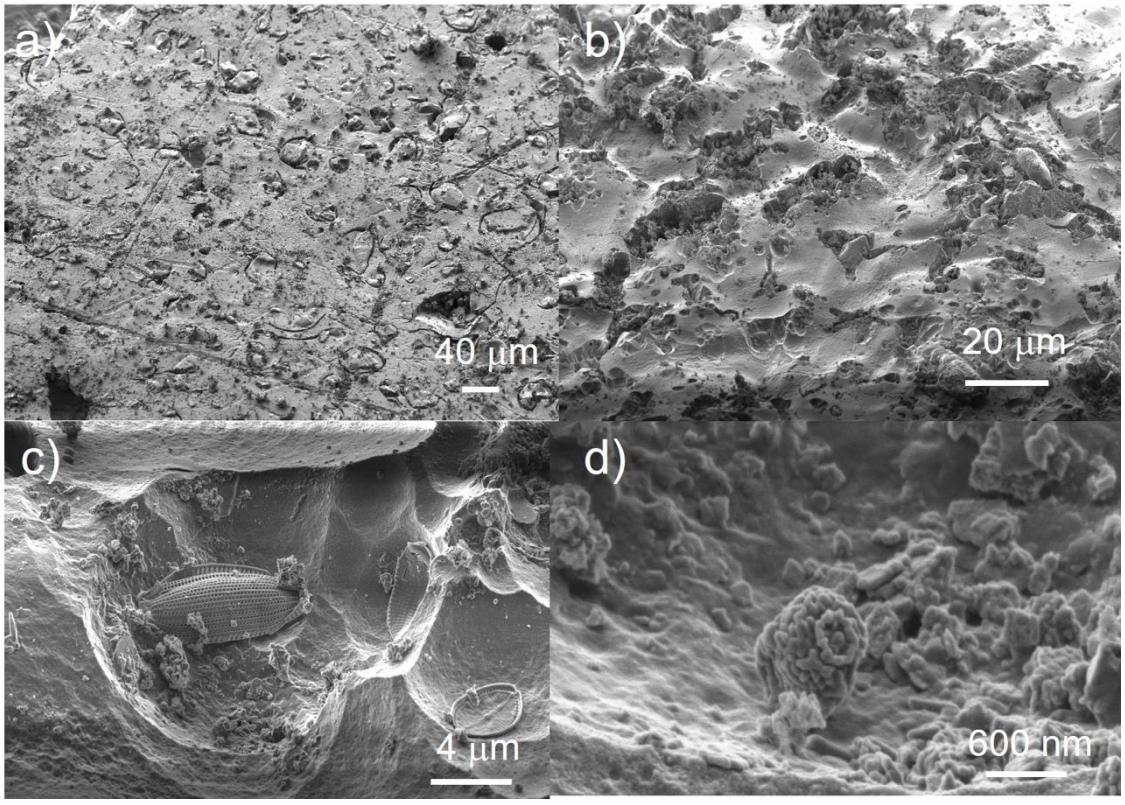

Figure 9.- Secondary electron images (2 kV) of the surface of samples of dish *C*: a) area of white glaze *C*-1; b), c) and d) area of blue glaze *C*-2.

Although mechanisms of transport and transformation of the silicic acid species into the diatom cells are not completely understood, several approaches have been proposed. These models demonstrate that certain proteins actively facilitate the uptake and transport of the dissolved silicic acid within the cell and participate in the intracellular mechanisms of synthesis of biogenic silica, the so-called silicification process of the diatoms [78,79]. It is generally accepted that the diatoms intracellularly synthesize the biogenic silica by polymerization of the silicic acid uptaken from the environment and then, this material is extruded towards the cell exterior forming a gel network that is added to the wall and finally conforms the frustules, the silica cell walls of diatoms, made of two valves called thecae.

According to the secondary electron images of the surface of dish *C*, the microcavities in whose sinus are deposited diatoms (Fig. 9b,c) could be formed by the metabolic activity of diatoms. Figure 10 shows a scheme of the growing of a diatom at expense of the glaze silica. In the first step ion exchange of network modifiers takes place in parallel to the

hydrolytic breaking of the siliceous network that results in the formation of nanoscopic pores in the surface of the glaze (Fig. 10a). An epitheca obtained as a result of the binary fission of the parent diatom can be deposited by Oceans currents on the surface of the glazed dish and, perhaps, on a small pore (Fig. 10b and Fig. 9c). The diatom in contact with the glaze surface traps the silicic acid molecules yielded in the hydrolytic breakdown of the network. These Si-containing molecules are used for forming the second frustule named hypotheca Fig. 10d and complete the structure of a mature diatom. It should be noted that diatoms preferably use the glaze matrix instead of the quartz or K-feldspar grains owing to the higher easiness for dissolving silicic acid in the former due to the presence of network modifiers which promote faster destruction of the Si-network through the ion exchange process.

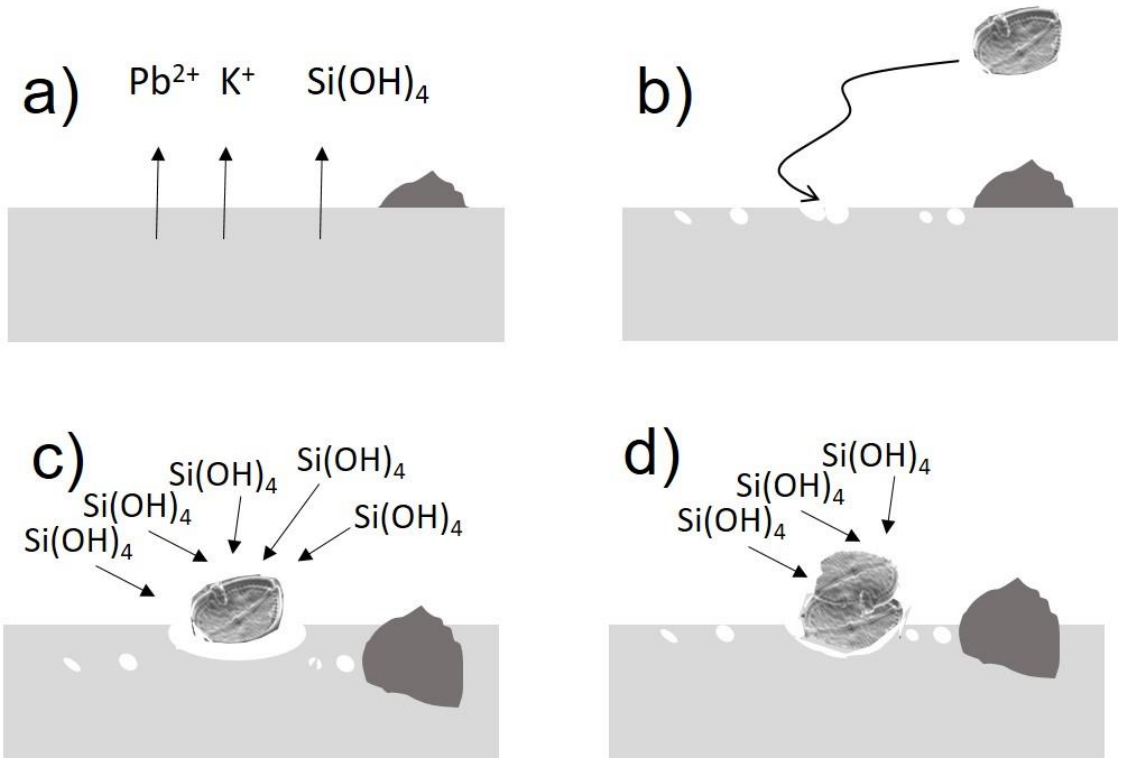

Figure 10.- Scheme of the growing of a diatom at expense of the glaze silica.

3.2 FTIR spectroscopy

The IR absorption spectra obtained in ATR mode in the unaltered glaze and the corrosion layers have yielded complementary data to describe the differential alteration processes that take place in the different environments. Tables 1S-3S list the main IR absorption bands identified in the corrosion layers and the uncorroded glazes of the three studied pieces *A, B,* and *C*. Overlapped bands in the range 1200 and 600 cm^{-1}, which are associated with the Si-network, have been transformed in the underlying individual bands after applying deconvolution and curve fitting processes on the original overlapped band. Percentages of the area of the underlying bands referred to the area of the deconvolved

band (100% area) have also been calculated and original, deconvolved, and underlying individual bands are illustrated in Figs. 7S-9S. Assignation of bands has been made according to prior studies on vibrational spectroscopic studies of alkali glazes and lead silicate glasses and their corrosion behavior [57,58,70,76,80-82].

3.2.1. Atmospheric environment

Fig. 11 shows the IR absorption spectra obtained in the unaltered glaze (a) and the corrosion layer (b) of samples taken from the *A*-1 white area of tile *A*. The uncorroded glaze is characterized by the silicate broad band in the range 1260-800 cm^{-1} with the maximum at 873 cm^{-1} assigned to the asymmetric stretching vibration of Si(Al)-O^{-}-R (R: network modifier) and shoulders at 1155 and 1016 cm^{-1} ascribed to stretching vibration of Si=O group and asymmetric stretching vibration of Si-O-Si and Si-O-Al (bonds between [SiO_4] and [AlO_4] tetrahedra in the glaze), respectively. Bands at 770 and 699 cm^{-1} are also identified that are associated with asymmetric stretching vibration of Si-O-Si(Al) and silico-oxygen and/or silicoaluminum-oxygen rings in the glaze, respectively. It is interesting to note that in the *A*-2 and *A*-3 yellow and orange samples a band at 672 cm^{-1} is occurring, which is assigned to the stretching vibration of the SbO_4 group of the lead antimonate pigment.

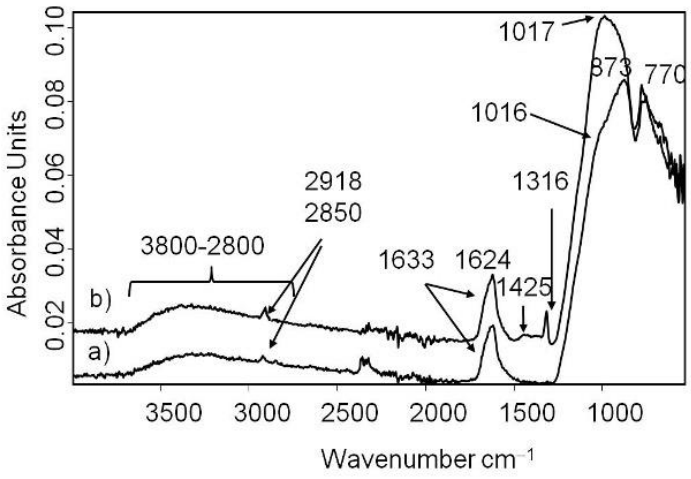

Figure 11.- IR absorption spectra acquired in the white area of tile *A*: a) unaltered glaze; b) corrosion layer.

The main changes in the glaze structure of the corroded layer are the slight intensity increment of the broad band between 3800-2800 and band at 1633 cm^{-1} assigned to –OH groups of silanol and surface water with different degrees of interaction and hydrogen bonding, which suggests a higher degree of hydration due to the aqueous external attack. An increase of the intensity of bands ascribed to Si=O and Si-O-Si and Si-O-Al bonds is also observed, which is characteristic of a silica-rich gel layer. Concomitantly, a blueshift of the maximum of the silicate band to 1017 cm^{-1} is observed that indicates the loss of

Si(Al)-O^--R due to the ion exchange and migration of the network modifiers. Other remarkable findings observed in the IR spectrum of the corrosion layer are the occurrence of new IR bands at 1624 and 1316 cm^{-1} ascribed to stretching vibrations of lead and calcium oxalates, band at 1425 cm^{-1} assigned to stretching vibration of carbonate group and increase of bands at 2918 and 2850 cm^{-1} associated with unspecific organic matter. The occurrence of these IR bands indicates that the corrosion layer contains abundant lead carbonate precipitated and organic matter infiltrated. In a subsequent alteration process, the organic matter has been transformed in Ca^{2+} and Pb^{2+} oxalates that remain also precipitated in the more open Si-network of the corrosion layer.

3.2.2. Burial environment

Fig. 12a shows the IR absorption spectrum acquired in the uncorroded glaze of the *B*-1 white area of the ceramic fragment *B*. Similarly to tile *A*, the silicate broad band of the uncorroded glaze is characterized by a maximum at 862 cm^{-1} and shoulders at 1155 and 963 cm^{-1} in the glaze. Bands at 766 and 692 cm^{-1} are also identified. IR bands at 3800-2800 and 1633 cm^{-1} of silanol and hydration are also recognized. In the IR spectrum of the amorphous corrosion layer (Fig. 12b) more intense IR bands at 3800-2800 and 1633 cm^{-1} denote the increase of the hydration degree and silanol groups in the layer. A band at 1427 cm^{-1} assigned to stretching vibration of carbonate group confirms the presence of precipitated carbonate salts mainly of lead. The alteration of the glaze structure in this corroded layer is confirmed by the intensification of the broad band between 3800-2800 cm^{-1} and band at 1633 cm^{-1} and by the blueshift of the maximum of the silicate band to 1033 cm^{-1}. Presence of a shoulder at 897 cm^{-1} suggests a partial loss of Si(Al)-O^--R for migration of the network modifiers. The increase of Si=O, Si-O-Si, and Si-O-Al bonds indicates the transformation of the glaze Si-network in a more open Si-rich gel layer.

Fig. 12c shows the IR absorption spectrum acquired in the outer lamellar layer. A more intense broad band between 3800-2800 and bands at 1633 and 1427 cm^{-1} are observed in this layer. The silicate band also undergoes changes associated with the blueshift of maximum and shoulders of underlying individual bands that move to 903, 1021, and 1167 cm^{-1}. These displacements confirm an almost complete loss of Si(Al)-O^--R groups for a notable migration of the network modifiers. The increase in the intensity of Si=O, Si-O-Si, and Si-O-Al bands confirms the transformation of the Si-network in an extremely open Si-rich gel layer.

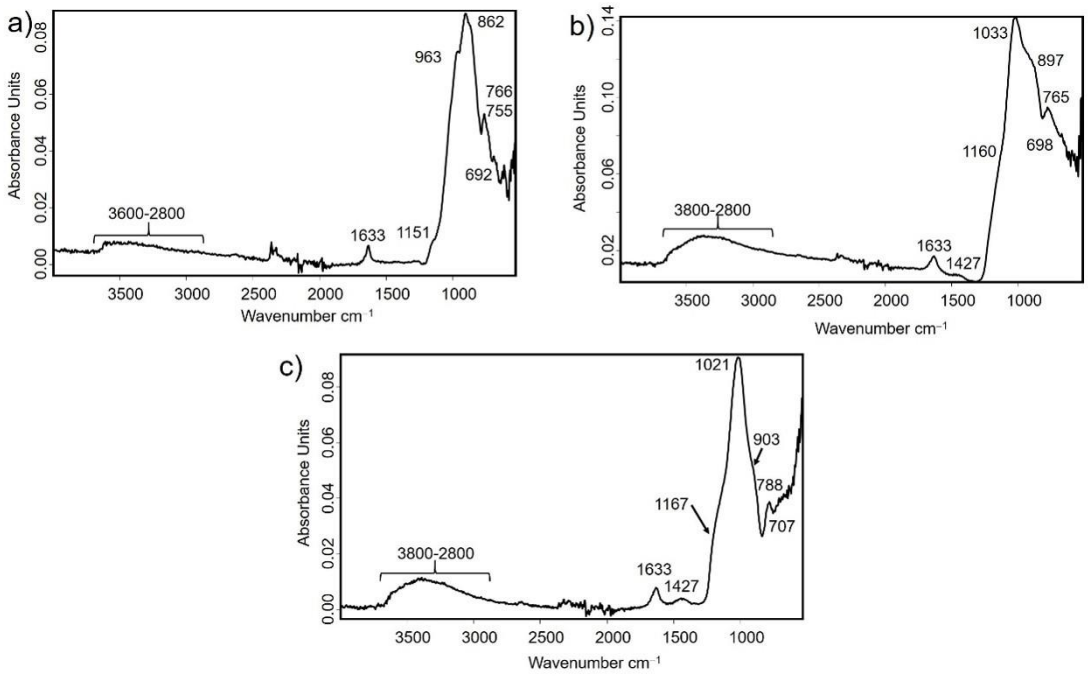

Figure 12.- IR absorption spectra acquired in the white area of fragment *B*: a) unaltered glaze; b) amorphous corrosion layer; c) lamellar corrosion layer.

3.2.3. Underwater environment

Fig. 13 shows the IR absorption spectrum acquired in the *C*-1 white area of the glaze of dish *C*. The silicate broad band of this glaze exhibits maximum at 925 and notable shoulder at 861 cm^{-1} and lesser intense shoulders at 1150 and 1068 cm^{-1}. It is remarkable the intensity of the band at 861 cm^{-1} as should be expected in an uncorroded glaze in agreement with the absence of corrosion layer observed in the examination with FIB-FESEM-EDX.

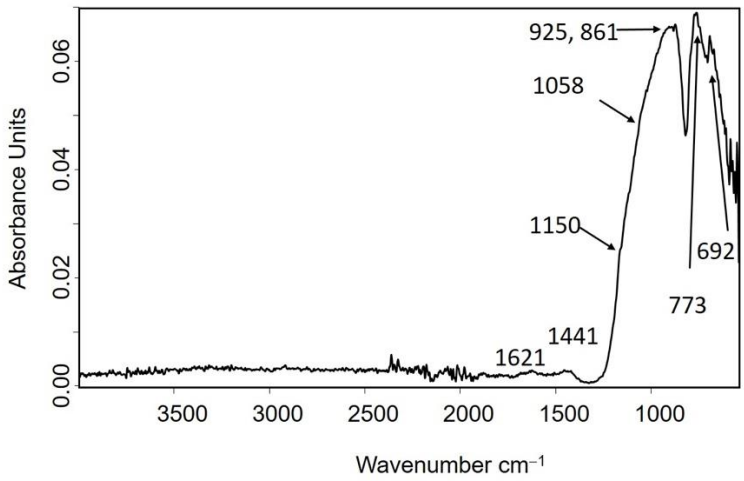

Figure 13.- IR absorption spectra acquired in the white area of tile *C*.

4. Conclusions

The FIB-FESEM-EDX technique has been applied in the study of the corrosion processes of archaeological glazed ceramic for the first time. This advanced microscopy technique has been successful in the identification of corrosion layers of nanoscopic thickness that could not be identified using the conventional examination of cross-sections using FESEM-EDX. In addition, X-ray microanalysis carried out on the trenches has provided compositional data at the nanoscale that allow establishing a comparison between the chemical composition of the corrosion layer and the uncorroded glaze.

The three selected glazed ceramic pieces are good examples of the differential corrosion mechanisms that take place depending on the environmental conditions. The atmospheric environment promotes the formation of a thin precipitation layer formed by lead carbonates and deposited organic materials that have been degraded to oxalate salts. The burial context has demonstrated a great degradative effect forming an amorphous gel layer that evolves to a thicker lamellar corrosion layer due to repeated seasonal humidity-dryness cycles. But the more interesting finding has been associated with the unusual and selective deteriorating effect on the marine matrix glaze due to the metabolic silicification activity of diatoms for forming their frustules during their growing and maturation. This effect has been reported for the first time in the present study.

Declaration of competing interest

The authors have declared no conflict of interest.

CRediT author statement

María Teresa Doménech Carbó: conceptualization, methodology, validation, investigation, resources, writing-original draft, writing-review & editing preparation, visualization, supervision, funding administration, funding acquisition. Carolina May-Cerovaz: resources, methodology, data curation, investigation, writing-review & editing preparation, visualization. Antonio Doménech-Carbó: methodology, formal analysis, investigation, writing-review & editing preparation, visualization.

5. Acknowledgments

This work was supported by the Spanish R+D+I Project PID2020-113022GB-I00 supported by MCIN/ AEI/10.13039/501100011033. The authors wish to also thank Mr. Manuel Planes, Dr. José Luis Moya, and Alicia Nuez-Inbernón, technical supervisors of the Electron Microscopy Service of the *Universitat Politècnica de València*. Authors also aknowledge the support by Mr Joaquín Bolufer-Marqués, Director of the Museo Arqueológico y Etnografico Soler Blasco of Xàbia (Spain) and Mr. Josep Pérez-Camps director of the *Museo de Cerámica de Manises* (Spain).

6. References

[1] M.S. Tite, I. Freestone, R. Mason, J. Molera, M. Vendrell-Saz, N. Wood, Lead glazes in antiquity-methods of production and reasons for use, Archaeometry 40 (1998) 241-260. https:// 10.1111/j.1475-4754.1998.tb00836.x.

[2] M.S. Walton, M.S. Tite, Production technology of Roman lead-glazed pottery and its continuance into late antiquity, Archaeometry 52 (2010) 733–759. https://10.1111/j.1475-4754.2009.00506.x.

[3] M. Tite, O. Watson, T. Pradell, M. Matin, G. Molina, K. Domoney, A. Bouquillon, Revisiting the beginnings of tin-opacified Islamic glazes, J. Archaeol. Sci. 57 (2015) 80-91, https:// 10.1016/j.jas.2015.02.005.

[4] R.B. Mason, M.S. Tite, The beginnings of tin-opacification of pottery glazes, Archaeometry 39 (1997) 41–58, https:// 10.1111/j.1475-4754.1997.tb00789.x.

[5] J. Molera, T. Pradell, L. Merino, M. García-Vallés, J. García-Orellana, N. Salvadó, M. Vendrell-Saz, M., La tecnología de la cerámica Islámica y mudéjar, Caesaraugusta 73 (1997) 15–41.

[6] M.S. Tite, The production technology of Italian maiolica: a reassessment, J. Archaeol. Sci. 36 (2009) 2065–2080, https://10.1016/j.jas.2009.07.006.

[7] E. Salinas, T. Pradell, The transition from lead transparent to tin-opacified glaze productions in the western Islamic lands: al-Andalus, c. 875–929 CE, J. Archaeol. Sci. 94 (2018) 1-11, https://10.1016/j.jas.2018.03.010, and references therein.

[8] J. Molera, J.C. Carvajal López, G. Molina, T. Pradell, Glazes, colourants and decorations in early Islamic glazed ceramics from the Vega of Granada (9th to 12th centuries CE), J. Archaeol. Sci. Reports 21 (2018) 1141–1151, https://10.1016/j.jasrep.2017.05.017.

[9] J. Molera, J. Coll, A. Labrador, T. Pradell, Manganese brown decorations in 10th to 18th century Spanish tin glazed ceramics, App. Clay Sci. 82 (2013) 86–90, https:// 10.1016/j.clay.2013.05.018.

[10] J. Molera, M. Vendrell-Saz, J. Pérez-Arantegui, Chemical and Textural Characterization of Tin Glazes in Islamic Ceramics from Eastern Spain, J. Archaeol. Sci. 28 (2001) 331-340, https://10.1006/jasc.2000.0606.

[11] J. Molera, M. García, T. Pradel, M. Vendrell-Saz, Hispano-moresque pottery production of the fourteenth century workshop of Testar del Molí (Paterna, Spain), Archaeometry 38 (1996) 67–80, https:// 10.1111/j.1475-4754.1996.tb00761.x

[12] J.G. Iñañez, R.J. Speakman, J. Buxeda i Garrigós, M.D. Glascock, Chemical characterization of tin-lead glazed pottery from the Iberian Peninsula and the Canary Islands: initial steps toward a better understanding of Spanish colonial pottery in the Americas, Archaeometry 51 (2009) 546–567. https:// 10.1111/j.1475-4754.2008.00431.x.

[13] J. Romero-Pastor, A. García-Porras, R. Van Grieken, S. Potgieter-Vermaak, J. Coll-Conesa, C. Cardell, New insights in technology characterization of medieval Valencia glazes, X-Ray Spectrom. 44 (2015) 426–435. https:// 10.1002/xrs.2613.

[14] J. Pérez-Arantegui, M. Resano, E. García-Ruiz, F. Vanhaecke, C. Roldán, J. Ferrero, J. Coll, Characterization of cobalt pigments found in traditional Valencian ceramics by means of laser ablation-inductively coupled plasma mass spectrometry and portable X-ray fluorescence spectrometry, Talanta 74 (2008) 1271–1280, https:// 10.1016/j.talanta.2007.08.044.

[15] J. Molera, M. Vendrell-Saz, M. Garcia-Valles, Technology and color development of Hispano-moresque lead-glazed pottery, Archaeometry 39 (1997) 23-39, https:// 10.1111/j.1475-4754.1996.tb00758.x.

[16] S. Coentro, L. C. Alves, C. Relvas, T. Ferreira, J. Mirão, J. Molera, The glaze technology of Hispano-moresque ceramic tiles: a comparison between Portuguese and Spanish collections, Archaeometry 59 (2017) 667–684, https:// 10.1111/arcm.12280.

[17] C. Fortina, A. Santagostino Barbone, I. Turbanti, Memmi Sienese 'archaic' majolica: a technological study of ceramic bodies and coatings, Archaeometry 47 (2005) 535–555, https:// 10.1111/j.1475-4754.2005.00218.x.

[18] L.F. Vieira Ferreira, D.P. Ferreira, D.S. Conceição, L.F. Santos, M.F.C. Pereira, T.M. Casimiro, I. Ferreira Machado, Portuguese tin-glazed earthenware from the 17th century. Part 2: A spectroscopic characterization of pigments, glazes and pastes of the three main production centers, Spectrochim. Acta A, 149 (2015) 285–294, https:// 10.1016/j.saa.2015.04.090.

[19] L.F. Vieira Ferreira, A. Gonzalez, M.F.C. Pereira, L.F. Santos, T.M. Casimiro, D.P. Ferreira, D.S. Conceição, I. Ferreira Machado, Spectroscopy of 16th century Portuguese tin-glazed earthenware produced in the region of Lisbon, Ceram. Int. 41 (2015) 13433-13446, http://dx.doi.org/10.1016/j.ceramint.2015.07.132.

[20] T.M. El-Shamy, J. Lewins, R.W. Douglas, The dependence on the pH of the decomposition of glasses by aqueous solutions, Glass Technol. 13 (1972) 77-80.

[21] J.M. Fernández-Navarro, El Vidrio, CSIC, Madrid, 1991, pp. 590–591.

[22] B.C. Bunker, Molecular mechanisms for corrosion of silica and silicate glasses, J. Non-Cryst. Solids 179 (1994) 300-308. https:// 10.1016/0022-3093(94)90708-0.

[23] B. Lamain, M.R. Van Bommel, G. Verhaar, N.H. Tennent, The development of an ion chromatography protocol for detecting the early stages of glass degradation, in: K. Van Lokeren Campagne, H. Römich (Eds.), Recent Advances in Glass, Stained-Glass, and Ceramics Conservation, Amsterdam, 7–10 October 2013, SPA Uitgevers, Zwolle, 2013, pp. 303–311.

[24] A. Rodrigues, S. Fearn, T. Palomar, M. Vilarigues, Early stages of surface alteration of soda-rich-silicate glasses in the museum environment, Cor. Sci. 143 (2018) 362–375. https://doi.org/10.1016/j.corsci.2018.08.012.

[25] A. Rodrigues, S. Fearn, M. Vilarigues, Historic K-rich silicate glass surface alteration: Behaviour of high-silica content matrices, Cor. Sci. 145 (2018) 249–261. https://doi.org/10.1016/j.corsci.2018.10.010.

[26] T. Palomar, D. de la Fuente, M. Morcillo, M. Alvarez de Buergo, M. Vilariguesa, Early stages of glass alteration in the coastal atmosphere, Build. Environ. 147 (2019) 305–313. https://doi.org/10.1016/j.buildenv.2018.10.034.

[27] H. Römich, Historic glass and its interaction with the environment, in: Tennent NH (Ed.), The conservation of glass and ceramics, Research, practice and training, James & James, London, 1999, pp 5–14.

[28] M. Vilarigues, R.C. da Silva, Ion beam and infrared analysis of medieval stained glass, Appl. Phys. A 79 (2004) 373–378, https:// 10.1007/s00339-004-2538-9.

[29] N. Carmona, M.A. Villegas, J.M.F. Navarro, Characterisation of an intermediate decay phenomenon of historical glasses, J. Mater. Sci. 41 (2006) 2339–2346, https://10.1007/s10853-005-3948-6.

[30] C.M. Jackson, D. Greenfield, L.A. Howie, An assessment of compositional and morphological changes in model archaeological glasses in an acid burial matrix, Archaeometry 54 (2012) 489–507, https:// 10.1111/j.1475-4754.2011.00632.x.

[31] M. Melcher, M. Schreiner, Leaching studies on naturally weathered potash-lime-silica glasses, J. Non-Cryst. Solids 352 (5) (2006) 368–379, https:// 10.1016/j.jnoncrysol.2006.01.017.

[32] A. Genga, M. Siciliano, L. Famà, E. Filippo, T. Siciliano, A. Mangone, A. Traini, C. Laganara, Characterization of surface layers formed under natural environmental conditions on medieval glass from Siponto (Southern Italy), Mater. Chem. Phys. 111 (2008) 480–485. https://10.1016/j.matchemphys.2008.04.057

[33] T. Palomar, Characterization of the alteration processes of historical glasses on the Seabed, Mater. Chem. Phys. 214 (2018) 391-401. https:// 10.1016/j.matchemphys.2018.04.107.

[34] F. Barbana, R. Bertoncello, L. Milanese, C. Sad, Alteration and corrosion phenomena in Roman submerged glass fragments, J. Non-Cryst. Solids 337 (2004) 136–141. https://10.1016/j.jnoncrysol.2004.03.118.

[35] M. Schreiner, Corrosion of historic glass and enamels, Compr. Anal. Chem. 42 (2004) 713-754, https:// 10.1016/S0166-526X(04)80020-5.

[36] G.E. De Benedetto, P. Acquafredda, M. Masieri, G. Quarta, L. Sabbatini, P.G. Zambonin, M. Tite, M. Walton, Investigation on roman lead glaze from Canosa: results of chemical analyses, Archaeometry 46 (2004) 615–624, https://10.1111/j.1475-4754.2004.00177.x.

[37] A. Machado, M. Vilarigues, Blue enamel pigment-Chemical and morphological characterization of its corrosion process, Cor. Sci. 139 (2018) 235–242, https://10.1016/j.corsci.2018.05.005.

[38] X. Yin, T.J. Huang, H. Gong, Chemical evolution of lead in ancient artifacts -A case study of early Chinese lead-silicate glaze, J. Eur. Ceram. Soc. 40 (2020) 2222-2228, https:// 10.1016/j.jeurceramsoc.2020.01.002.

[39] Y. Zhou, Y. Hu, Y. Tao, J. Sun, Y. Cui, K. Wang, D. Hu, Study on the microstructure of the multilayer glaze of the16th-17th century export blue-and-white porcelain excavated from Nan'ao-I Shipwreck, Ceram. Int. 42 (2016) 17456–17465, https:// 10.1016/j.ceramint.2016.08.050.

[40] A. Doménech-Carbó, M.T. Doménech-Carbó, J.V. Gimeno-Adelantado, M. Moya-Moreno, y F. Bosch-Reig, Identification of lead (II) and (IV) in mediaeval glazes by cyclic voltammetry and differential pulse voltammetry. Application to the study of alterations in archaeological ceramic, Electroanalysis, 12 (2000) 120-127, https:// 10.1002/(SICI)1521-4109(200002)12:2<120.

[41] A. Doménech-Carbó, M.T. Doménech-Carbó Electrochemical Characterization of Archaeological Tin-Opacified Lead-Alkali Glazes and Their Corrosion Processes, Electroanalysis 17 (2005) 1959–1969, https:// 10.1002/elan.200503322.

[42] M.T. Doménech-Carbó, A. Doménech-Carbó, L. Osete-Cortina, M.C. Saurí-Peris, A Study on Corrosion Processes of Archaeological Glass from the Valencian Region (Spain) and its Consolidation Treatment, Mikrochim. Acta, 154 (2006) 123-142, https:// 10.1007/s00604-005-0472-y.

[43] A. Doménech-Carbó, M.A. Villegas, F. Agua, M.T. Doménech-Carbó, B. Martínez-Ramírez, Electrochemical fingerprint of archaeological lead silicate glasses from the voltammetry of microparticles approach, J. Am. Ceram. Soc., 99 (2016) 3915-3923, https://10.1111/jace.14430.

[44] W.H. Zachariasen, The atomic arrangement in glass, J. Am. Chem. Soc. 54 (1932) 3841-3851, https:// 10.1021/ja01349a006.

[45] M. Leventhal, P. J. Bray, Nuclear magnetic resonance investigations of compounds and glasses in the systems PbO-$B2O_3$ and PbO-SiO_2, Phys. Chem. Glasses 6 (1965) 113-125.

[46] J. Roqué-Rosell, A. Pinto, C. Marini, J. Prieto Burgos, J. Groenen, M. Campeny, Ph. Sciau, Synchrotron XAS study of Mn and Fe in Chinese blue-and-white Ming porcelains from the second half of the 15th century, Ceram. Int. 47 (2021) 2715–2724, https://doi.org/10.1016/j.ceramint.2020.09.123.

[47] C. De Vito, L. Medeghini, S. Garruto, F. Coletti, I. De Luca, S. Mignardia, Medieval glazed ceramic from Caesar's Forum (Rome, Italy): Production technology, Ceram. Int. 44 (2018) 5055–5062, https://doi.org/10.1016/j.ceramint.2017.12.104.

[48] S. Polić, S.Ristić, J.Stašić, M.Trtica, B.Radojković Studies of the Iranian medieval ceramic surface modified by pulsed tea CO2 and Nd:YAG lasers, Ceram. Int. 41 (2015) 85-100, http://dx.doi.org/10.1016/j.ceramint.2014.08.036.

[49] J. Wen, Z. Chen, Q. Zeng, L. Hu, B. Wang, J. Shi, G. Zhang, Multi-micro analytical studies of blue-and-white porcelain (Ming dynasty) excavated from Shuangchuan island, Ceram. Int. 45 (2019) 13362–13368, https://doi.org/10.1016/j.ceramint.2019.04.031.

[50] Y. Xu, Y. Qin, F. Ding, Characterization of the rare oil spot glazed bowl excavated from the Xiao kiln site of north China, Ceram. Int. 43 (2017) 8636-8642, http://dx.doi.org/10.1016/j.ceramint.2017.03.177.

[51] R. Zhang, I. Garachon, P. Gethin, J. van Campen, Double layers glaze analysis of the Fujian export blue-and-white porcelain from the *Witte Leeuw* shipwreck (1613), Ceram. Int. 46 (2020) 13474-13481, https://doi.org/10.1016/j.ceramint.2020.02.131.

[52] S. Saber-Samandari, K. Alamara, S. Saber-Samandaric, Calcium phosphatecoatings: Morphology, micro-structure and mechanical properties, Ceram. Int. 40 (2014) 563-572, http://dx.doi.org/10.1016/j.ceramint.2013.06.038.

[53] H. Berek, C.G. Aneziris, Effect of focused ion beam sample preparation on the phase composition of zirconia, Ceram. Int. 44 (2018) 17643–17654, https://doi.org/10.1016/j.ceramint.2018.06.226.

[54] T. Pradell, R. Fernandes, G. Molina, A.D. Smith, J. Molera, A. Climent-Font, M.S. Tite, Technology of production of Syrian lustre (11th to 13th century), J. Eur. Ceram. Soc. 38 (2018) 2716–2727, https://doi.org/10.1016/j.jeurceramsoc.2018.01.046.

[55] G. Molina, M.S. Tite, J. Molera, A. Climent-Font, T. Pradell, Technology of production of polychrome lustre, J. Eur. Ceram. Soc. 34 (2014) 2563–2574, http://dx.doi.org/10.1016/j.jeurceramsoc.2014.03.010.

[56] M.T. Doménech-Carbó, F. di Turo, N. Montoya, F. Catalli, A. Doménech-Carbó, C. de Vito, FIB-FESEM and EMPA results on Antoninianus silver coins for manufacturing and corrosion processes, Sci. Rep. 8 (2018) 10676, https://10.1038/s41598-018-28990-x

[57] M.T. Doménech-Carbó, C. Álvarez-Romero, A. Doménech-Carbó, L. Osete-Cortina, M. L. Martínez-Bazán, Microchemical surface analysis of historic copper-based coins by the combined use of FIB-FESEM-EDX, OM, FTIR spectroscopy and solid-state electrochemical techniques, Microchem. J. 148 (2019) 573-581, https:// 10.1016/j.microc.2019.05.039.

[58] S. Amma, S.H. Kim, C.G. Pantano, Analysis of Water and Hydroxyl Species in Soda Lime Glass Surfaces Using Attenuated Total Reflection (ATR)-IR Spectroscopy, J. Am. Ceram. Soc. 99 (2016) 128–134. https:// 10.1111/jace.13856.

[59] S. Amma, J.W. Luo, C.G. Pantano, S.H. Kim, Specular reflectance (SR) and attenuated total reflectance (ATR) infrared (IR) spectroscopy of transparent flat glass surfaces: a case study for soda lime float glass. J. Non-Cryst. Solids 428 (2015) 189–96, https:// 10.1016/j.jnoncrysol.2015.08.015.

[60] H. Liu, S.H. Hahn, M. Ren, M. Thiruvillamalai, Searching for correlations between vibrational spectral features and structural parameters of silicate glass network, J. Am. Ceram. Soc. 103 (2020) 3575-3589, https:// 10.1111/jace.17036.

[61] M.T. Doménech-Carbó, Y. Lee, L. Osete-Cortina, S. Marín-Rey. Influence of plasticizer and biocide on the functional properties of gelatin-based adhesives used in painting consolidation, J. Adhes. Sci. Technol. 29 (2015) 1774-1795, https:// 10.1080/01694243.2014.975999.

[62] R. Padilla, O. Schalm, K. Janssens, R. Arrazcaeta, P. Van Espen, Microanalytical characterization of surface decoration in Majolica pottery, Anal. Chim. Acta 535 (2005) 201–211, https://10.1016/j.aca.2004.11.082.

[63] J. Molera, T. Pradell, T., N. Salvadó, M. Vendrell-Saz, Evidence of tin oxide recrystallization in opacified lead glaze, J. Am. Cer. Soc. 82 (1999) 2871–2875, https:// 10.1111/j.1151-2916.1999.tb02170.x.

[64] W. D. Kingery, M. Aronson, On the technology of Renaissance maiolica glazes, Faenza, 5 (1990) 226–35.

[65] B. Bajnóczi, G. Nagy, M. Tóth, I. Ringer, A. Ridovics, Archaeometric characterization of 17th-century tin-glazed Anabaptist, (Hutterite) faience artefacts from North-East-Hungary, J. Archaeol. Sci. 45 (2014) 1-14, https://doi.org/10.1016/j.jas.2014.01.030.

[66] J. W. Allan, Abu 'l Qasim's treatise, Iran, 11 (1973) 111–20.

[67] M. Tite, T. Pradell, A. Shortland, Discovery, production and use of tin-based opacifiers in glasses, enamels and glazes from the late iron age onwards: a reassessment, Archaeometry 50 (2008) 67–84, https://10.1111/j.1475-4754.2007.00339.x.

[68] Sánchez Ramos, S., Bosch Reig, F., Gimeno Adelantado, J.V., Yusá Marco, D.J., Doménech Carbó, A., 2002. Study and dating of medieval ceramic tiles by analysis of enamels with atomic absorption spectroscopy, X-ray fluorescence and electron probe microanalysis. Spectrochim. Acta B. 57, 689–700, https://doi.org/10.1016/S0584-8547(01)00395-0.

[69] R. Ali Rahimi, S.K. Sadrnezhaad, G. Raisali, Chemical durability of lead silicate glass in HNO_3, HCl and H_2SO_4 aqueous acid solutions, J. Non-Cryst. Solids 355 (2009) 169–174. https://doi.org/10.1016/j.jnoncrysol.2008.11.001.

[70] F.H. El-Batal, E.M.A. Khalil, Y.M. Hamdy, H.M. Zidan, M.S. Aziz, A.M. Abdelghany, Infrared reflection spectroscopy for precise tracking of corrosion behavior in 3D-transition metals doped binary lead silicate glass, Physica B 405 (2010) 2648–2653, https://doi.org/10.1016/j.physb.2010.03.044.

[71] M. Vilarigues, P. Redola, A. Machado, P.A. Rodrigues, L.C. Alves, R.C. da Silva Corrosion of 15th and early 16th century stained glass from the monastery of Batalha studied with external ion beam, Mater. Charact. 62 (2011) 211-217, https://doi.org/10.1016/j.matchar.2010.12.001.

[72] A. Xie, Y. Shen, D. Ma, F. Huang, L. Qiu, S. LiL. Chen, Growth of calcium oxalate crystals induced by complex films containing biomolecules, Cryst. Res. Technol. 42 (2007) 667–72, https:// 10.1002/crat.200610886.

[73] J. Pérez-Arantegui, B. Montull, M. Resano, J.M. Ortega, Materials and technological evolution of ancient cobalt-blue-decorated ceramics: Pigments and work patterns in tin-glazed objects from Aragon (Spain) from the 15th to the 18th century AD, J. Eur. Ceram. Soc. 29 (2009) 2499–2509, https://doi.org/10.1016/j.jeurceramsoc.2009.03.004.

[74] E. De Pauw, P. Tack, E. Verhaeven, S. Bauters, L. Acke, B. Vekemans, L. Vincze, Microbeam X-ray fluorescence and X-ray absorption spectroscopic analysis of Chinese blue-and-white kraak porcelain dating from the Ming dynasty, Spectrochim. Acta B 149 (2018) 190–196, https://doi.org/10.1016/j.sab.2018.08.006.

[75] C. Schultz-Münzenberg, W. Meisel, P. Gütlich, Changes of lead silicate glasses induced by leaching, J. Non-Cryst. Solids, 238 (1998) 83-90, https://doi.org/10.1016/S0022-3093(98)00580-8.

[76] C. Bonnet, A. Bouquillon, S. Turrell, V. Deram, B. Mille, J. Salomon, J.H. Thomassin, C. Fiaud, Alteration of lead silicate glasses due to leaching in heated acid solutions, J. Non-Cryst. Solids, 323 (2003) 214–220, https://10.1016/S0022-3093(03)00279-5.

[77] R. Bertoncello, L. Milanese, A. Bouquillon, J.-C. Dran, B. Mille, J. Salomon, Leaching of lead silicate glasses in acid environment: compositional and structural changes, Appl. Phys. A 79 (2004) 193–198, https:// 10.1007/s00339-004-2651-9.

[78] R.K. Iler, The Chemistry of Silica: Solubility, Polymerization, Colloid and Surface Properties, and Biochemistry, Wiley-Interscience, New York, 1979.

[79] M. Hildebrand, S.J.L. Lerch, R.P. Shrestha, Understanding Diatom Cell Wall Silicification—Moving Forward, Front. Mar. Sci. 5 (2018) 125, https:// 10.3389/fmars.2018.00125.

[80] G. Li, H. Ji, Ch. Lv, N. Li, Y. Hong, L. Zhang, Aging study on the modern imitation glaze and ancient glaze of the Ming and Qing dynasties based on FTIR decomposition spectra, J. Non-Cryst. Solids 505 (2019) 102–108, https://: doi.org/10.1016/j.jnoncrysol.2018.10.024

[81] M. Sitarz, The structure of simple silicate glasses in the light of Middle Infrared spectroscopy studies, J. Non-Cryst. Solids 357 (2011) 1603–1608, https://10.1016/j.jnoncrysol.2011.01.007.

[82] C.A. Worrell, T. Henshall, Vibrational spectroscopic studies of some lead silicate glasses, J. Non-Cryst. Solids 29 (1978) 283-299, https:// 10.1016/0022-3093(78)90150-3.

Application of focused ion beam-field emission scanning electron microscopy-X-ray microanalysis in the study of the surface alterations of archaeological tin-glazed ceramics

María Teresa Doménech-Carbó[a*], Carolina Mai-Cerovaz[a], Antonio Doménech-Carbó[b]

[a]Institut Universitari de Restauració del Patrimoni, Universitat Politècnica de València, Camino de Vera s/n, 46022 Valencia, Spain
[b]Departament de Química Analítica, Universitat de València, Avda. Dr Moliner s/n, 46100 Burjassot, Spain

Corresponding author: tdomenec@crbc.upv.es

Keywords: archaeological tin-glazes, FIB-FESEM-EDX, FTIR spectroscopy, optical microscopy, glaze corrosion process

Abstract

The historical evolution of tin-glazed ceramics is a subject that has attracted the attention of many scientists and, consequently, abundant archaeometrical studies can be found in the specialized literature. Nevertheless, a lesser number of studies aimed at the characterization of the alterations undergone by archaeological glazes has been reported. This work describes some unusual alteration processes found in tin-glazes depending on the environmental conditions surrounding the piece during centuries. For this purpose, focused ion beam-field emission scanning electron microscopy-X-ray microanalysis (FIB-FESEM-EDX), an advanced instrumental technique for surface analysis at the nanoscale, has been used for the first time, complementarily to optical microscopy (OM), FESEM-EDX and Fourier transform Infrared spectroscopy (FTIR). In the buried glaze the nanostructure of the outer lamellar corrosion layer due to humidity-dryness cycles is described. Unusual and selective erosion of the glaze matrix due to the silicification metabolism of diatoms is observed in a submarine glaze. A nanometric outer corrosion layer formed by precipitated corrosion products and unspecific organic matter that has been partially degraded to lead and calcium oxalates is found in a glazed tile subjected to an atmospheric environment.

1. Introduction

Lead and tin-glazes have been widely produced since antiquity for decorating tiles and earthenware pottery due to their ability for improving the utilitarian qualities of ceramic objects by making them impervious to liquids and providing a bright. Additionally, the glazes interact properly with most metal oxides used to provide color (i.e. titanium, vanadium, chromium, manganese, iron, cobalt, nickel, or copper).

The chemical composition of lead and tin-glazes has been varying over time. First glazes were prepared as alkali glazes with a PbO low content of 1-2 %. The lead content was progressively increased to that of a lead-alkali glaze (20-40 % PbO and 5-12 % alkali) achieving a value of 55 % PbO and 3 % alkali in Hispano-Moresque pottery [1].

Concerning studies of alteration processes, abundant literature is found describing alteration mechanisms of glass [2-17]. Nevertheless, lesser works devoted to the study of the alteration processes of ceramic glazes are found. De Benedetto et al. [18], identify a corrosion layer in Roman green lead-glazes but they do not provide the chemical composition of this corrosion layer. Salinas and Pradell [19] mention a lead leaching process accompanied by recrystallization of lead and calcium phosphates and carbonates inside surface cracks in lead transparent glazes made in al-Andalus (c. 875–929 AD). Similarly, Molera et al. [20] found cerussite in an outer corrosion layer formed in buried manganese brown glazes from Murcia (Spain, tenth century). Machado and Vilarigues [21] study the corrosion process of blue enamels on laboratory specimens that mimic old enamels used for decorating windows. The analyses were performed by using inductively coupled plasma-atomic emission spectroscopy (ICP-AES), Fourier Transform Infrared Spectroscopy (FTIR), X-ray diffraction (XRD), and Fibre Optic Reflectance Spectroscopy (FORS), and confirmed that alkali ions are leached promoting a change of the chemical structure of the glaze matrix with the formation of Co^{2+}/Co^{3+} spinel crystals. Lixiviation of Pb^{2+} ions with recrystallization as cerussite and hydrocerussite in the surface was also described in this research. Yin et al. [22] found lead leaching in buried lead-based glazes from the Han dynasty (206 BC-220 AD) that resulted in the formation of a lamellar Si-rich layer near the surface and an outer crystalline layer of precipitated lead carbonate. This analytical study used transmission and scanning electron microscopies (TEM, SEM), X-ray microanalysis (SEM-EDX), FTIR, and XRD. Zhou et al. [23] found underwater blue-and-white porcelain affected by devitrification, a process that resulted in a multi-layered outer structure. In prior papers, Doménech-Carbo et al. [24-27], using solid-state electrochemical techniques, found a corrosion layer with lower lead content due to significant lixiviation of alkaline and Pb^{2+} ions present in buried glasses and tin-glazes as network modifiers.

The preparation of cross-sections by the conventional metallographic procedure is a method abundantly employed in the study of archaeological glazes and porcelains [28-33]. Focused ion beam (FIB) is a novel technique that is being increasingly used as a preparation method of ultra-polished cross-sections and lamellae for the investigation of microstructure and phase transformation of materials related to ceramics using electron

backscattered diffraction (EBSD) [34], and transmission electron microscopy (TEM) [35], respectively. Nevertheless, FIB, as a preparative technique, has been solely used for studying the nanostructure of lusterware [36,37] and corrosion layers in copper-based coins [38,39]. This work presents a study in which the novel technique of FIB is coupled to a FESEM-EDX (FIB-FESEM-EDX) for performing surface analysis at nanoscale combined with OM and FTIR spectroscopy in the study of the surface corrosion exhibited by tin-glazed ceramics that have remained for centuries in different environments. To the knowledge of the authors, corrosion processes occurring in ceramic glazes have not still been studied utilizing FIB-FESEM-EDX.

2. Material and methods

2.1. Description of archaeological pieces

Three glazed ceramic pieces that exhibited alteration processes have been selected taking into consideration the influence of the environmental conditions to which the pieces were subjected during centuries: a) polychromed tin-glazed tile *A* (Valencia workshop, 18th century); b) fragment of blue and white tin-glazed dish *B* (Manises workshop, 15th century) and c) fragment of blue and white tin-glazed dish *C* (Xàbia workshop, 19th century). A summary of the glazed ceramic characteristics and samples analyzed are presented as electronic supplementary material (ESM) in Table 1S. Images of the ceramic pieces are shown in Fig. 1.

2.2. Instrumentation

- Optical microscope Leica M165 stereo microscope using a capture system of high-resolution digital image IC80HD controlled by LAS software.

- FIB-FESEM Zeiss (Orsay Physics Kleindiek Oxford Instruments) model Auriga compact equipment. The operating conditions were: 30 kV, and current intensities of 500 µA, and 20 nA in the FIB for generating the focused beam of Ga ions that enabled the sectioning of samples and formation of trenches. The Ga beam impacts perpendicularly to the plane of the vertical wall of the trench by tilting 54° the stage where is placed the ceramic microsample. Secondary electron images were acquired at 2 kV in the FESEM. Spot and area analyses were performed in cross-sections and trenches operating with an Oxford-X Max X-ray microanalysis system coupled to the FESEM controlled by Aztec software. A voltage of 20 kV and a working distance of 6-7 mm was used. ZAF method for semiquantitative microanalysis was applied. The counting time for acquiring X-ray spectra was 100 s. A more detailed description of the working conditions can be found as ESM.

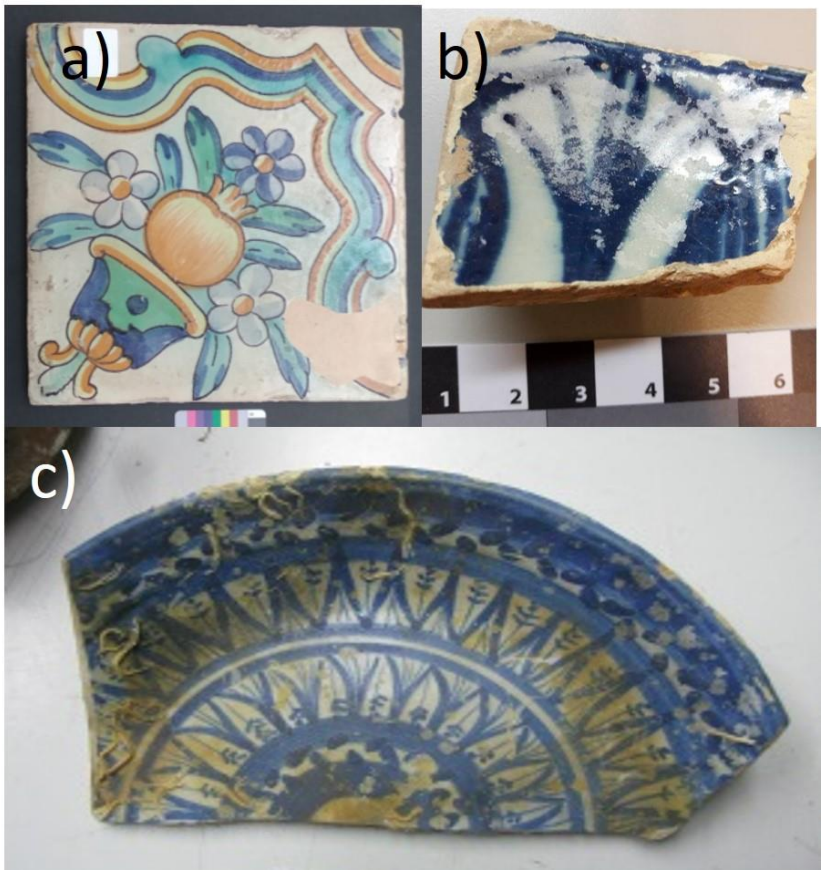

Figure 1.- a) Polychromed tin-glazed tile *A* (Valencia workshop, 18th century); b) fragment of blue and white tin-glazed dish *B* (Manises workshop, 15th century); c) fragment of blue and white tin-glazed dish *C* (Xàbia workshop, 19th century).

- Vertex 70 Fourier-transform infrared spectrometer with an FR-DTGS (fast recovery deuterated triglycine sulfate) temperature-stabilized coated detector and an MKII Golden Gate Attenuated Total Reflectance (ATR) accessory. 32 scans were collected at a resolution of 4 cm^{-1} and the IR spectra acquired were processed with OPUS/IR 7.2 software. Deconvolution and curve-fitting analysis were applied to the IR overlapped bands of silicate group in the range 1260-600 cm^{-1}. The methodology applied has been described elsewhere [40]. Other experimental working conditions are included as ESM.

2.3. Preparation of samples for the analyses

The chemical analyses of this study were carried out on microsamples (surface area lesser than 1 mm^2) excised from the glaze of the ceramic pieces using scalpels. Sampling points were selected with the help of an optical microscope to avoid areas with fissures, cracks, and other superficial irregularities in all the glazed pieces and earth deposits in the burial fragments. The microsamples excised from the glazes were prepared in three different modes: as trenches and as cross-sections for OM and FESEM-EDX analysis and

mechanically handled for ATR-FTIR analysis (see ESM for preparation details of the two latter).

Trenches were formed using the FIB on microsamples excised from the glazes. The microsamples were fixed with carbon adhesive to the aluminum stage of the FESEM. The size of the trenches was (10x8 μm). Points for performing the trenches in the glaze microsamples, whose surface exhibited a homogeneous appearance, were chosen avoiding areas where cracks, pits, fissures, or mineral microdeposits were present (Figure 1S in ESM). Microsamples were firstly carbon-coated and, after this, a second treatment was carried out that consisted of applying a thin layer of Pt on the area where the trench should be performed to protect the surface of the glaze at the nanoscale from possible alterations due to the Ga ions bombardment during the formation of the trench. Figure 2 shows the electron image of the corrosion layer from a corroded glaze sample of fragment *B*. The poor lamellar morphology observed in Fig. 2a is due to the hardness of the metallographic preparation of the cross-section. It contrasts with the fine structure observed at the nanoscale in Fig. 2b obtained on a trench with the FIB preparation.

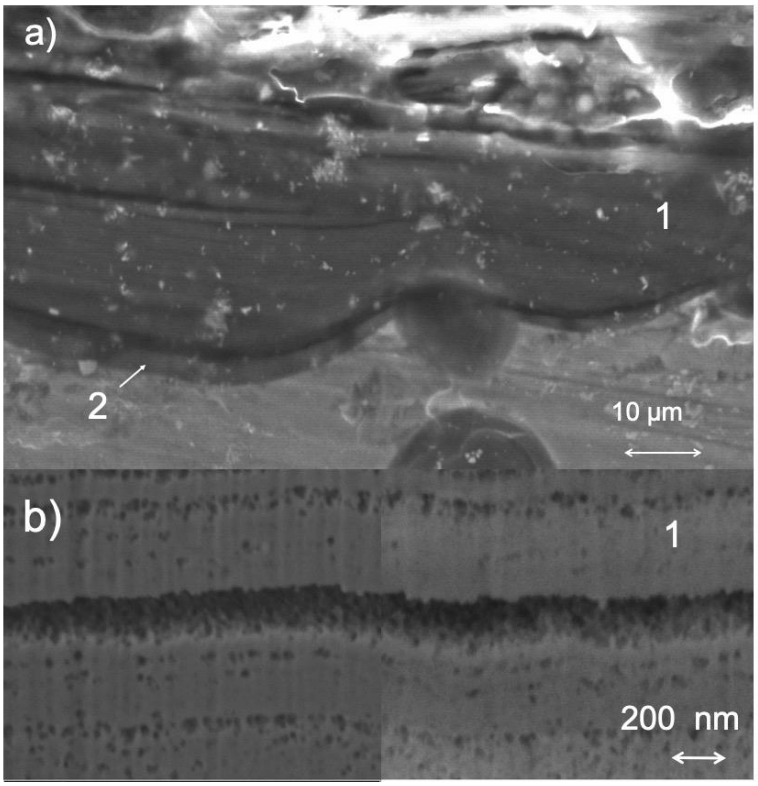

Figure 2. a) Backscattered electron image of the cross-section prepared with the conventional metallographic method, (1) outer lamellar corrosion sublayer and (2) inner amorphous corrosion sublayer; b) secondary electron image obtained in a trench formed with FIB. Detail of the nanoporous structure of the lamellae in sublayer (1).

3. Results and discussion

3.1 Atmospheric environment

3.1.1. Results

Microsamples excised from six areas in tile *A*, which represent the white glaze and the colors used by the craftsman, were analyzed. At the naked eye, the surface of the tile had a glassy shine denoting an apparent absence of glaze corrosion (a more detailed description of the state of conservation of the glaze can be found as ESM, Fig. 2S and 3S). Table 1 summarizes the average composition of the uncorroded bulk of the glaze obtained in the cross-section of the white glaze using FESEM-EDX. According to the classification established by Tite et al. [1], this glaze can be considered a lead alkali glaze with a 21 % PbO and total alumina, alkali, and alkaline earth oxides content of 16.5 %. The pigments identified using the X-ray microanalysis were Naples yellow for yellow, manganese oxides, zaffre, and mixed copper green (see ESM for a more detailed description).

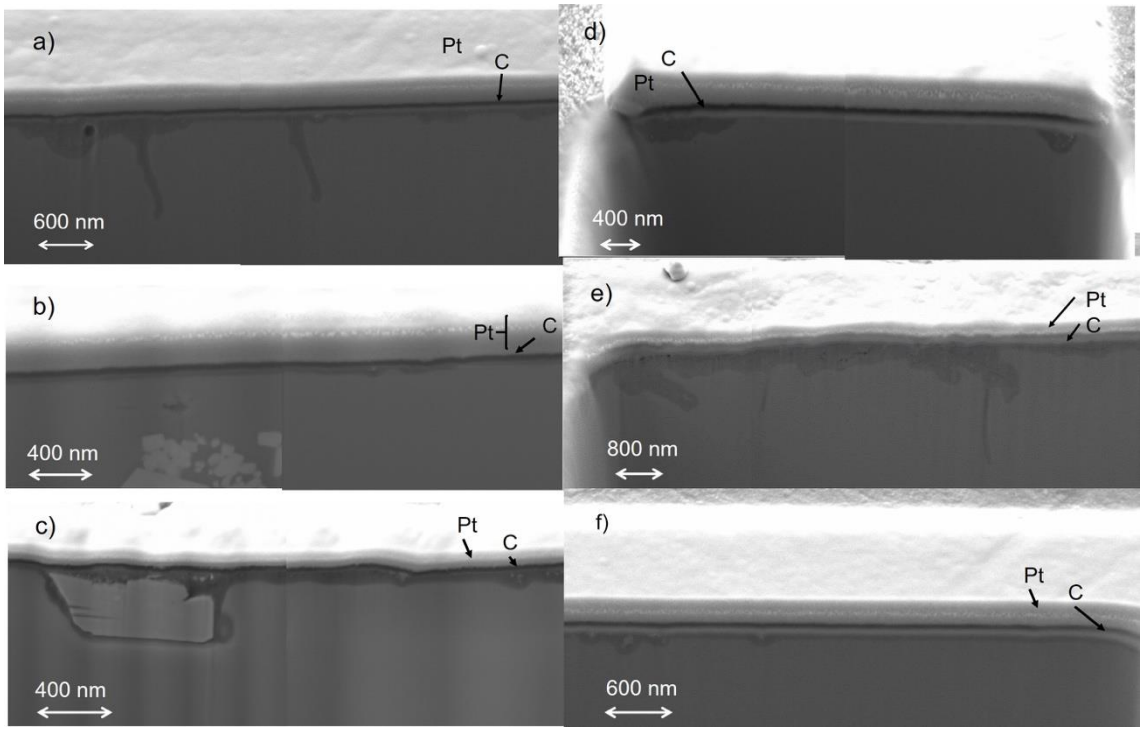

Figure 3.- Secondary electron image (2 kV) of the outer part of the trenches performed in the different colored areas of the surface of the glaze of tile *A*. Detail of the thin corrosion layer formed in the glaze can be seen in all the trenches: a) brown; b) orange; c) yellow; d) green; e) blue; f) white.

Fig. 3 shows in detail the outer part of the FIB trenches formed in the six microsamples taken from the different colored areas of the tile. A dark grey thin corrosion layer is observed on the surface of all glazes. Brown and blue glazes (Figs. 3a,e) show the thickest corrosion layers (30-500 nm). Some pore and infiltration channels 1.3-2 μm deep are also

observed for which, presumably, the corrosion process advances towards the glaze core. The corrosion layer appears as broad isolated spots on the surface of the green glaze (Fig. 3d). Glazes orange, yellow, and white (Fig. 3b,c,f) exhibit a thinner corrosion layer that achieves a minimum thickness of 25 nm in the orange sample. A few nanometric cassiterite crystals and pores are recognized in the corrosion layer of these glazes. The corrosion layer is surrounding a big grain of Naples yellow in the yellow glaze (Fig. 3c). It can also be seen abundant subangular grains of lead antimonate with variable sizes under 2 μm mixed with small grains of cassiterite in the subsurface of the orange glaze (Fig. 3b).

As it is shown in Table 1, X-ray spectra acquired in the trenches, in both corrosion layer and uncorroded inner glaze, confirmed that silica content increases in the corrosion layer. A low shift in the content values of network modifier ions is also found. Potassium and magnesium content slightly diminish, which confirms the diffusion of these network modifiers from the uncorroded glaze. In contrast, a higher content is found for lead and calcium in the corrosion layer, which suggests that precipitation processes are taking place.

The presence of carbonates, mainly, calcium and lead carbonates as well as calcium and lead oxalates in the corrosion layer of tile *A* has been confirmed by FTIR spectroscopy. Figure 4a shows the IR absorption spectra obtained in the unaltered glaze (black line) and the corrosion layer (red line) of samples taken from the *A*-1 white area of tile *A*. Table 2S lists the main IR absorption bands identified in the corrosion layers and the uncorroded glazes of the *A* glaze. Assignation of bands has been made according to prior studies on vibrational spectroscopic studies of alkali glazes and lead silicate glasses and their corrosion behavior [39,41-46].

The main changes in the glaze structure of the corroded layer are the slight intensity increment of the broad band between 3800-2800 and band at 1633 cm^{-1} assigned to –OH groups of silanol and surface water with different degrees of interaction and hydrogen bonding, which suggests a higher degree of hydration due to the aqueous external attack. An increase of the intensity of bands ascribed to Si=O and Si-O-Si and Si-O-Al bonds (bonds between [SiO_4] and [AlO_4] tetrahedra in the glaze), is also observed, which is characteristic of a silica-rich gel layer. Concomitantly, a blueshift of the maximum of the silicate band from 873 cm^{-1} to 1017 cm^{-1} is observed that indicates the loss of Si(Al)-O^{-}-R (R: network modifier) due to the ion exchange and migration of the network modifiers (see also deconvolved bands in Figure 4S). Other remarkable findings are the occurrence of new IR bands at 1624 and 1316 cm^{-1} ascribed to lead and calcium oxalates, band at 1425 cm^{-1} assigned to carbonates and bands at 2918 and 2850 cm^{-1} associated with unspecific organic matter.

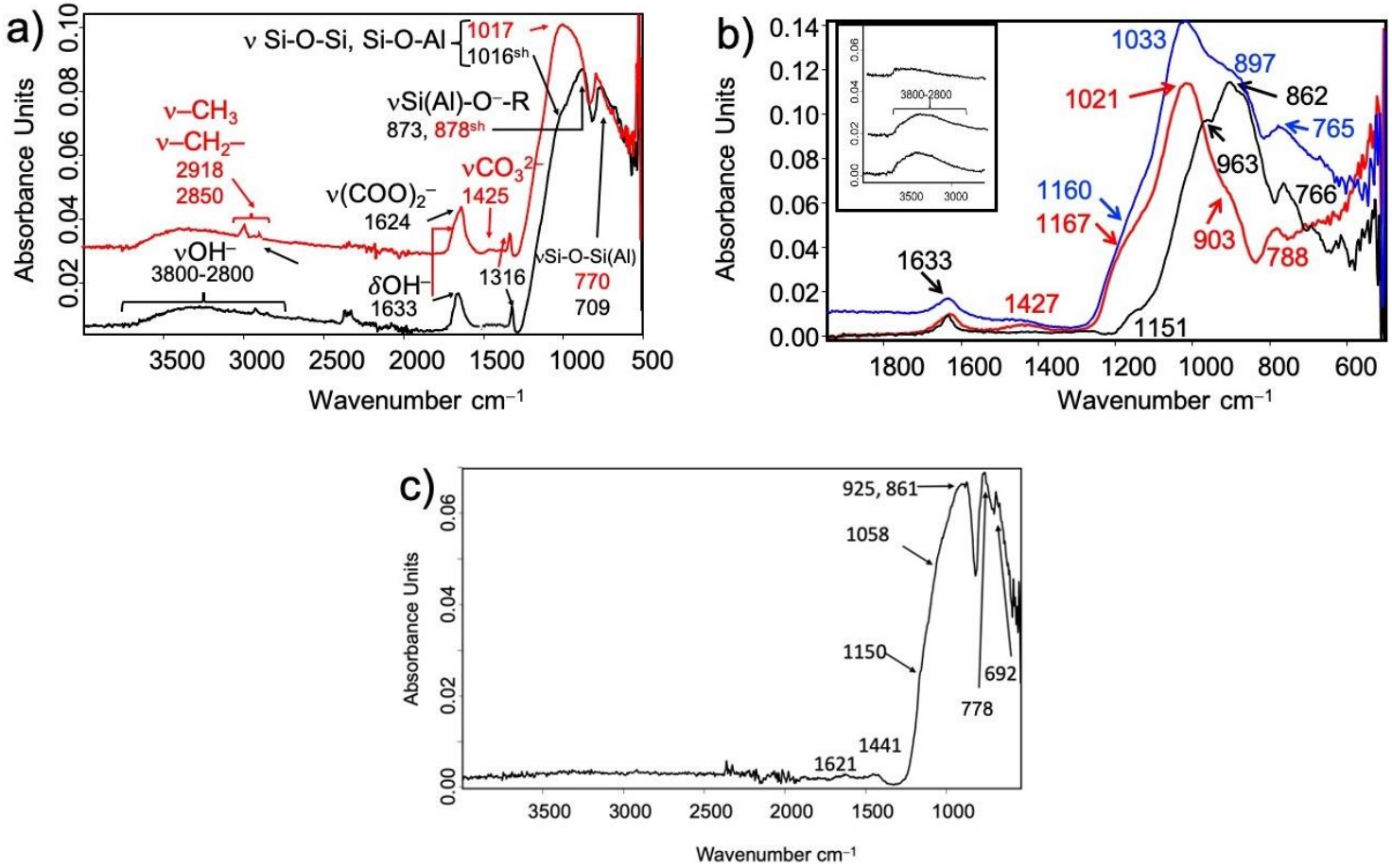

Figure 4.- IR absorption spectra acquired in: a) the white glaze area of tile *A*: unaltered glaze (black line); b) corrosion layer (red line); b) the white glaze area of fragment *B*: unaltered glaze (black line), amorphous inner corrosion layer (blue line), lamellar outer corrosion layer (red line); c) white glaze area of dish *C*.

Table 1.- Chemical compositions measured in the cross-section of the white area of tile (*A*-1) and the trenches formed in samples of the different colors of tile *A* using FIB-FESEM-EDX. Standard deviation in brackets.

Component		Chemical composition (% oxide)											
	Cross-section	Trench											
	A-1	A-1		A-2		A-3		A-4		A-5		A-6	
	Glaze*	G.M.	C.L.	G.M.	C.L.	G.M.	C.L.	G.M.	C.L.	G.M.	C.L.	G.M.	C.L.
Na_2O	0.4(0.1)	n.d.	0.30(0.01)	n.d.	0.4(0.1)	n.d.	n.d.	n.d.	n.d.	n.d.	1.0(0.1)	n.d.	0.5(0.3)
MgO	0.5(0.1)	n.d.	0.41(0.03)	n.d	n.d.	0.4(0.1)	0.7(0.1)	n.d.	n.d.	n.d.	0.3(0.1)	n.d.	0.46(0.03)
Al_2O_3	2.7(0.2)	1.4(0.1)	0.97(0.2)	1.1(0.1)	0.9(0.1)	1.3(0.2)	1.6(0.1)	1.1(0.1)	1.0(0.1)	1.3(0.1)	1.0(0.1)	1.46(0.03)	1.4(0.1)
SiO_2	55.1(0.9)	51.6(0.5)	52.3(0.4)	51(0.4)	52(0.3)	44(1)	48(1)	53(1)	58(1)	61(1)	62(1)	52.2(0.7)	54.4(0.4)
Cl	n.d.	n.d.	n.d.	n.d.	n.d.	n.d.	n.d.	n.d.	n.d.	n.d.	0.3(0.1)	n.d.	n.d.
K_2O	10.6(1)	13.8(0.2)	10.9(0.3)	9.3(0.03)	9.6(0.02)	9.3(0.2)	8.7(0.1)	10.4(0.1)	7.9(0.3)	10.7(0.1)	9.8(0.2)	13.2(0.6)	10.7(0.4)
CaO	2.7(0.5)	3.4(0.3)	3.7(0.3)	2.2(0.1)	2.7(0.1)	4.4(0.2)	3.9(0.1)	3.0(0.2)	3.5(0.3)	2.8(0.1)	3.2(0.1)	3.1(0.1)	3.2(0.3)
MnO	n.d.	n.d.	n.d.	n.d.	n.d.	n.d.	n.d.	0.5(0.1)	n.d.	n.d.	n.d.	n.d.	n.d.
FeO	n.d.	n.d.	n.d.	n.d.	n.d.	4.5(0.1)	3.6(0.1)	0.5(0.1)	n.d.	0.3(0.1)	0.4(0.1)	n.d.	0.1(0.3)
CoO	n.d.	n.d.	n.d.	n.d.	n.d.	n.d.	n.d.	n.d.	n.d.	1.1(0.1)	n.d.	n.d.	n.d.
As_2O_3	n.d.	n.d.	n.d.	n.d.	n.d.	n.d.	n.d.	n.d.	n.d.	0.03(0.1)	n.d.	n.d.	n.d.
CuO	0.8(0.6)	n.d.	n.d.	n.d.	n.d.	0.8(0.1)	n.d.	1.0(0.1)	n.d.	n.d.	n.d.	2.6(0.2)	2.3(0.1)
SnO	6.2(1)	2.9(0.4)	2.5(0.8)	2.1(0.1)	1.7(0.1)	n.d.	n.d.	3.6(0.2)	n.d.	2.6(0.1)	1.7(0.1)	n.d.	n.d.
Sb_2O_3	n.d.	n.d.	n.d.	n.d.	n.d.	7.4(0.2)	4.3(0.1)	n.d.	n.d.	n.d.	n.d.	n.d.	n.d.
PbO	21(1)	27.0(0.4)	28.9(0.9)	34(1)	36(1)	28(1)	30(1)	27(1)	29(1)	20(1)	21(1)	25.1(0.4)	27.1(0.7)

G.M.: glassy matrix of the glaze; C.L.: corrosion layer; n.d.: non detected; * Average composition measured in the cross-section.

3.1.2. Discussion

These results can be interpreted in light of general models of glass corrosion. Environmental humidity generates water microdrops that attack the glaze and result in ion exchange of network modifiers. In particular, the ion exchange of the Pb^{2+}network modifier ions goes by the process:

$$2(Si–O)–Pb + 2H^{+} \rightarrow 2(Si–OH) + Pb^{2+} \quad (1)$$

In parallel, hydrolysis of the silicate groups takes place forming silanol groups that distort and progressively open the structure of the network with the concomitant loss of cohesion. These processes result in a modification of the pH of the attacker solution [3]. The most open and porous silica-rich gel layer formed favors the infiltration of external ions and the reaction of atmospheric carbon dioxide with the dissolved ions forming insoluble carbonates and bicarbonates of calcium and lead, that remain retained in the porous structure of the gel layer [21,42,47,48]. On the other hand, the metabolic action of microorganisms can promote the occurrence of oxalate salts from the organic matter infiltrated [10,48,49].

3.2. Burial environment

3.2.1. Results

The altered areas of the surface of fragment *B* exhibit an iridescent aspect (see Fig. 5S). due to a corrosion layer recognized in cross-section in both white and blue glazes (see Fig 2 and Fig. 6S). This layer, in turn, comprises two sublayers (see arrows in Fig. 2). The upper one (1 in Fig 2a,b) exhibits a lamellar structure whereas the inner one (2 in Fig. 2a) has an amorphous morphology. These corrosion sublayers can be studied in more detail in the FIB trenches formed in both blue and white areas, which are shown in Fig. 5. The lamellar sublayer (Fig. 5b,d) has a minimum thickness in the range of 20-30 μm whereas the thinner amorphous sublayer (Fig. 5a,c) has a thickness ranging between 1600-340 nm. It is interesting to note that the abundant presence of nanopores formed on the lamellae (Fig. 2b) as well as on the top of the amorphous sublayer could be observed uniquely in the trenches due to the finest polishing of the cross-section achieved with the FIB technique.

Average chemical compositions obtained on the uncorroded glazes, the amorphous and lamellar corrosion layers are listed in table 2. The more remarkable changes are the progressive increase of the silica and tin oxide content from the uncorroded glaze to the amorphous and lamellar sublayers. The former indicates that ion exchange and hydrolysis reactions have taken place extensively. The increase of the tin oxide content is due to the high insolubility of the cassiterite microcrystals that remain trapped in the corrosion layers. A notable decrease in the content of lead oxide is also found from the uncorroded to the corroded layers.

Fig. 4b shows the IR absorption spectrum acquired in the uncorroded glaze of the *B*-1 white area of the ceramic fragment *B*. Similarly to tile *A*, the silicate broad band of the uncorroded glaze is characterized by a maximum at 862 cm^{-1} and shoulders at 1155 and 963 cm^{-1} in the glaze. In the IR spectrum of the amorphous corrosion layer (blue line) more intense IR bands at 3800-2800 and 1633 cm^{-1} denote the increase of the hydration degree and silanol groups in the layer. The band at 1427 cm^{-1} confirms the presence of precipitated carbonate salts mainly of lead. The alteration of the glaze structure in this corroded layer is confirmed by the intensification of the blueshift of the maximum of the silicate band to 1033 cm^{-1}. Presence of a shoulder at 897 cm^{-1} suggests a partial loss of Si(Al)-O^{-}-R for migration of the network modifiers. The increase of Si=O, Si-O-Si, and Si-O-Al bonds indicates the transformation of the glaze Si-network in a more open Si-rich gel layer. The IR absorption spectrum acquired in the outer lamellar layer (red line) shows a more intense broad band between 3800-2800 and bands at 1633 and 1427 cm^{-1}. The silicate band also undergoes changes associated with the blueshift of maximum and shoulders of underlying deconvolved individual bands that move to 903, 1021, and 1167 cm^{-1} (see also Fig. 7S). These displacements confirm an almost complete loss of Si(Al)-O^{-}-R groups for a notable migration of the network modifiers. The increase in the intensity of Si=O, Si-O-Si, and Si-O-Al bands confirms the transformation of the Si-network in an extremely open Si-rich gel layer.

3.2.2. Discussion

These results suggest that most of the lead present as mobile Pb^{2+} network modifier ions have migrated outside. The fraction of lead that remains in the corroded layers is supposed to be present as Pb^{4+} network former and as lead carbonate insoluble salts formed in the more open Si-enriched network of the corrosion sublayers. A low decrease of content is also observed in the rest of the elements from the uncorroded glaze to the outer lamellar sublayer with a slight increase in the latter sublayer in some of them. This result suggests that most of these mobile ions have been lixiviated with partial precipitation to insoluble salts in the outer sublayer.

The results obtained confirm that the corrosion mechanism is similar to that described previously for buried lead glasses [22,42,43,47,50,51]. The seasonal humidity-dryness cycles in the soil promote, in a first step, an enrichment in silica of the corrosion layer. Progressively the corrosion layer acquires abundant porosity that, concomitantly, promotes the penetration of the attacker solution containing exogenous ions such as H^{+} and CO_3^{2-}. The H^{+} ions favor the advance of the hydrolysis reaction whereas the leached Pb^{2+} ions can combine with CO_3^{2-} ions and precipitate forming lead carbonate that remains infiltrated in the lamellar layer and, in extreme instances, forms an outer precipitation layer of cerussite and hydrocerussite. During the dryness step the processes pass slowly forming an interlaminar space of a few hundred nanometers and the sequence starts again with the new humidity step in which the attacker solution penetrates forming a new lamella.

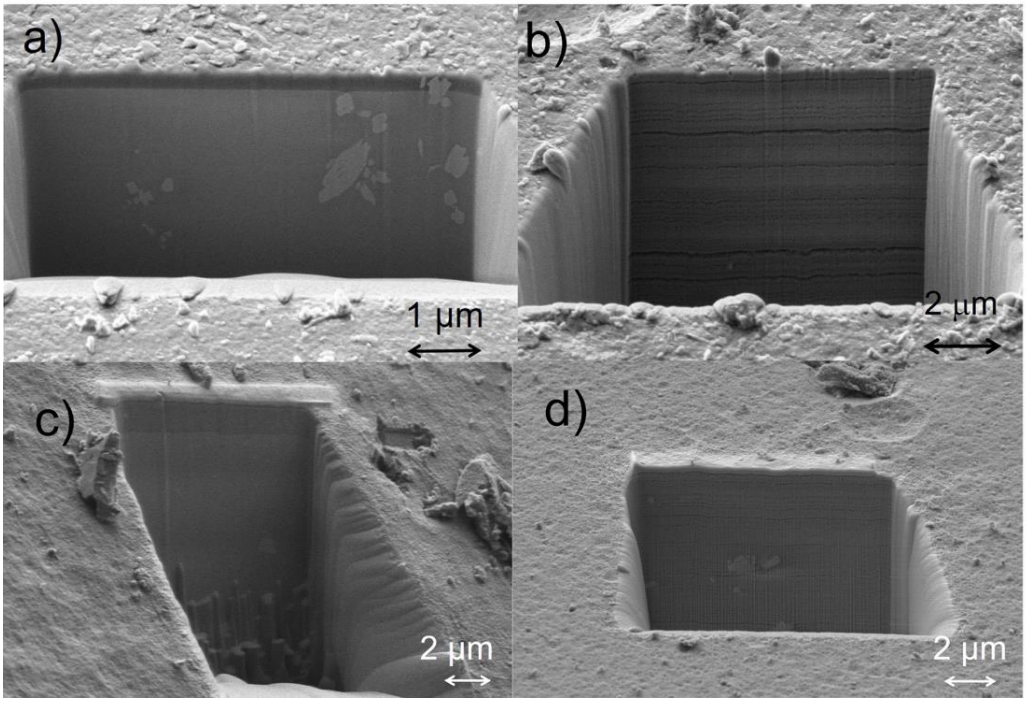

Figure 5.- Secondary electron image (2 kV) of the trenches performed in the colored areas of the glaze of fragment *B*: a) area of blue glaze *B*-2 with an amorphous layer of corrosion; b) area of blue glaze *B*-2 with an outer lamellar layer of corrosion; c) area of white glaze *B*-1 with an amorphous layer of corrosion; d) area of white glaze *B*-1 with an outer lamellar layer of corrosion.

Table 2.- Chemical compositions measured in the cross-section and the trenches formed in samples of the two colors of fragment *B* using FIB-FESEM-EDX. Standard deviation in brackets.

	Chemical composition (% oxide)							
	Cross-section		**Trench**					
Component	**Glaze***		**B-1 white**			**B-2 blue**		
	B-1	**B-2**	**G.M.**	**A.C.L.**	**L.C.L.**	**G.M.**	**A.C.L.**	**L.C.L.**
Na_2O	0.7(0.1)	0.6(0.1)	n.d.	n.d.	n.d.	0.3(0.3)	0.3(0.4).	0.6(0.1)
MgO	n.d.	n.d.	n.d.	n.d.	n.d.	n.d.	n.d.	0.2(0.4)
Al_2O_3	2.5(0.2)	2.1(0.2)	1.8(0.1)	5.2(0.1)	3.6(0.2)	2,0(0.1)	5.6(0.2)	5.7(0.5)
SiO_2	41(1)	40(1)	41(1)	56(1)	60(1)	43(1)	63(2)	66(3)
Cl	n.d.	n.d.	n.d.	n.d.	0.3(0.1)	n.d.	n.d.	n.d.
K_2O	6.0(0.3)	6.1(0.2)	10.9(0.3)	9.3(0.2)	8.7(0.1)	6.4(0.3)	5.3(0.3)	5.2(0.3)
CaO	2.2(0.2)	2.8(0.3)	4.1(0.2)	3.9(0.2)	2.7(0.2)	3.3(0.2)	2.4(0.3)	2.9(0.1)
FeO	n.d.	2.2(0.1)	3.9(0.2)	1.1(0.1)	1.5(0.1)	2.1(0.5)	3.0(0.2)	1.1(0.1)
CoO	n.d.	1.0(0.1)	n.d.	n.d.	n.d.	0.9(0.3)	n.d.	n.d.
SnO	11,4(0,5)	7.7(0.7)	5.9(0.1)	6.1(0.1)	18.4(0.1)	1,0(0.2)	5.0(0.4)	15(1)
PbO	36(1)	38(1)	35(1)	23(1)	8(1)	41(1)	16(1)	5(1)

G.M.: glassy matrix of the glaze; A.C.L.: amorphous gel layer of corrosion; L.C.L.: lamellar corrosion layer; n.d.: non detected; * Average composition measured in the cross-section.

3.3. Underwater environment

3.3.1. Results

Dish *C* exhibited alterations notably different from those found in the two prior pieces examined. The observation with a light microscope showed in detail the significant erosion undergone by the glaze that looked micro rough surface (Figure 8S). The cross-section was characterized by the abundant presence of bubbles and large grains of raw materials mainly quartz and K-feldspar. The thickness of the glazes is in the range of 235-560 µm (see Figs. 9S and 10S). The average values of oxide wt% content of the glaze obtained in the cross-section (see table 3) are in good agreement with the composition of tin lead-alkali glazes according to the classification of Tite et al., [1].

Figure 6 shows the trenches formed on samples of white (*C*-1) and blue (*C*-2) glaze areas of the dish. Average values of the chemical composition obtained in the trenches are listed in table 3. It is interesting to note that no corrosion layer was found in both samples.

Fig. 4c shows the IR absorption spectrum acquired in the *C*-1 white area of the glaze of dish *C*. The silicate broad band of this glaze exhibits maximum at 925 and notable shoulder at 861 cm^{-1} and lesser intense shoulders at 1150 and 1058 cm^{-1} (see deconvolved bands in Fig. 11S). It is remarkable the intensity of the band at 861 cm^{-1} as should be expected in an uncorroded glaze in agreement with the absence of corrosion layer observed in the examination with FIB-FESEM-EDX.

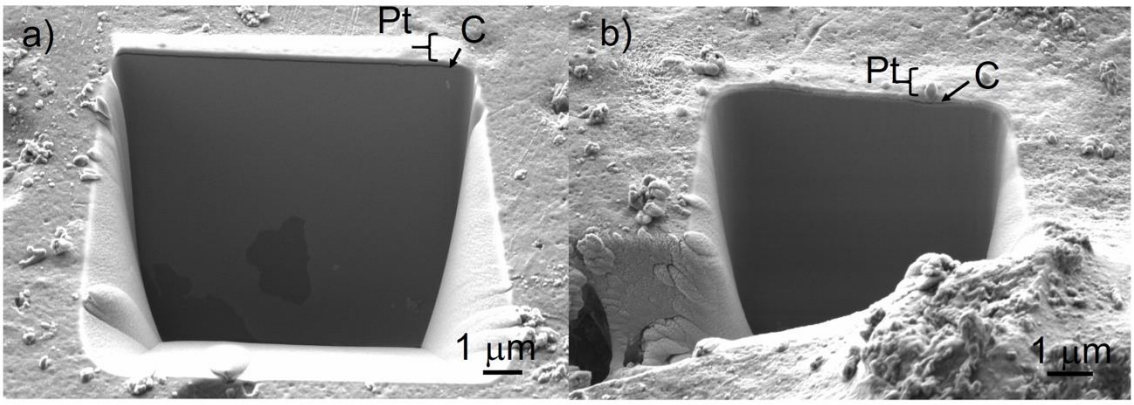

Figure 6.- Secondary electron images (2 kV) of the trenches formed in samples of dish *C*: a) area of white glaze *C*-1; b) area of blue glaze *C*-2.

Table 3. Chemical compositions measured in the cross-section and the trenches formed in samples of the two colors of the fragment *C* using FIB-FESEM-EDX. Standard deviation in brackets.

Component	Chemical composition (% oxide)			
	Cross-section		Trench	
	Glaze*		C-1 white	C-2 blue
	C-1	C-2	G.M.	G.M.
Al_2O_3	3.9(0.2)	3.7(0.2)	2.98(0.2)	2.1(0.2)
SiO_2	55(1)	53(1)	51.3(0.2)	49.7(0.2)
K_2O	5.8(0.2)	5.7(0.2)	5.9(0.2)	6.2(0.2)
CaO	2.0(0.3)	1.3(0.3)	n.d.	2.7(0.1)
CoO	n.d.	0.2(0.1)	n.d.	0,13(0.05)
SnO	2.0(0,3)	4.4(0.3)	2.1(0.1)	0.3(0.1)
PbO	31(1)	31(1)	36(1)	38(1)

G.M.: glassy matrix of the glaze; n.d.: non detected; * Average composition measured in the cross-section.

3.3.2. Discussion

From a morphological point of view, it is remarkable the absence of corrosion layer in the glaze surface, that makes a difference between the behavior of tin-glazes exposed to marine and those others in burial or atmospheric environments. The absence of a corrosion layer can be interpreted in the light of the high ability of the seawater for dissolving the Si-network. The general models for deterioration of glass and glazes in contact with aqueous solutions establish that the attack of the aqueous solution results in the hydrolytic breaking of the ≡Si–O–Si ≡ superficial network groups according to the reaction [3]:

$$\equiv Si–O–Si \equiv + H^+ + OH^- \rightarrow \equiv Si–OH + HO–Si \equiv + H^+ \qquad (2)$$

In parallel, another mechanism starts, which results in the ion exchange of network modifiers, mainly Pb^{2+} and K^+, in the case of the studied tin-glazes of the lead potash-rich type, according to the reaction (1). These processes promote the progressive destruction of the network and the formation of soluble silicic acid ($Si(OH)_4$) [3]. In marine solutions with high ionic strength, like that of the Mediterranean sea, the silicic acid molecules remain isolated or form small aggregates so that they can be assimilated by some aquatic microorganisms such as diatoms. This hypothesis is sustained by the secondary electron images obtained on the surface of the glazes. Figs. 7a,b show abundant unmelted grains of raw materials (quartz and K-feldspar) that are protruding the glassy matrix due to their higher resistance to chemical marine deteriorating agents.

Fig. 7a,b also shows concave sockets and broad fissures filled with abundant microcrystals as well as linear and curved marks that are associated with microorganisms'

activity. The former can be better understood in Figs. 7c,d where are identified microorganisms of navicular diatom type, of fusiform morphology (Fig. 7c), and other globular algae (Fig. 7d). It is interesting to note that the diatoms are located in the sinus of the concave sockets.

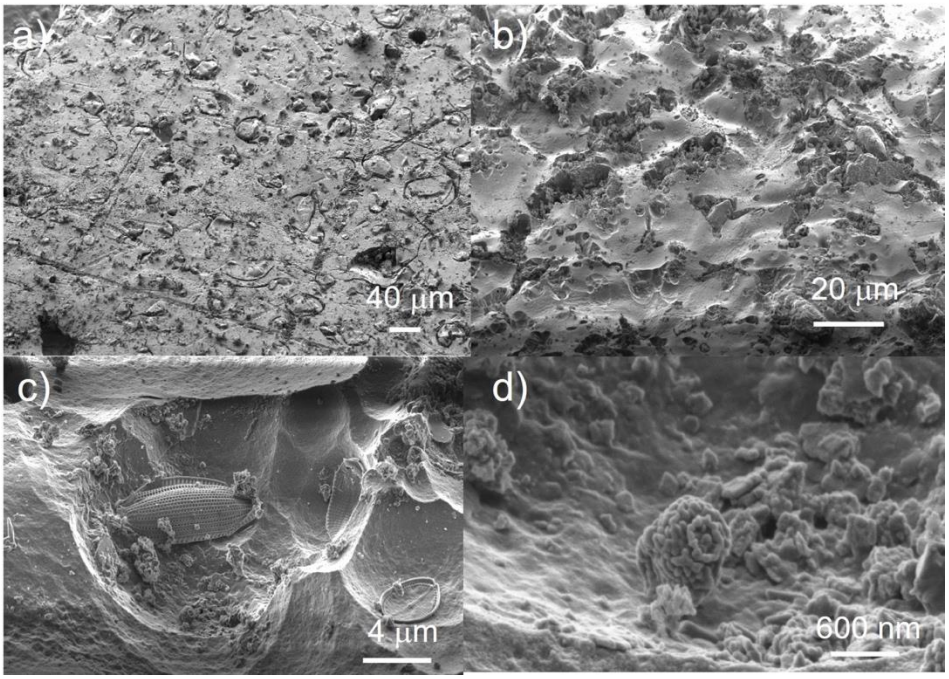

Figure 7.- Secondary electron images (2 kV) of the surface of samples of dish *C*: a) area of white glaze *C*-1; b), c) and d) area of blue glaze *C*-2.

Although mechanisms of transport and transformation of the silicic acid species into the diatom cells are not completely understood, several approaches have been proposed. These models demonstrate that certain proteins actively facilitate the uptake and transport of the dissolved silicic acid within the cell and participate in the intracellular mechanisms of synthesis of biogenic silica, the so-called silicification process of the diatoms [52,53]. It is generally accepted that the diatoms intracellularly synthesize the biogenic silica by polymerization of the silicic acid uptaken from the environment and then, this material is extruded towards the cell exterior forming a gel network that is added to the wall and finally conforms the frustules, the silica cell walls of diatoms, made of two valves called thecae.

According to the secondary electron images of the surface of dish *C*, the microcavities in whose sinus are deposited diatoms (Fig. 7b,c) could be formed by the metabolic activity of diatoms. Figure 8 shows a scheme of the growing of a diatom at expense of the glaze silica. In the first step ion exchange of network modifiers takes place in parallel to the hydrolytic breaking of the siliceous network that results in the formation of nanoscopic pores in the surface of the glaze (Fig. 8a). An epitheca obtained as a result of the binary fission of the parent diatom can be deposited by Oceans currents on the surface of the glazed dish and, perhaps, on a small pore (Fig. 8b and Fig. 7c). The diatom in contact

with the glaze surface traps the silicic acid molecules yielded in the hydrolytic breakdown of the network. These Si-containing molecules are used for forming the second frustule named hypotheca Fig. 8d and complete the structure of a mature diatom. It should be noted that diatoms preferably use the glaze matrix instead of the quartz or K-feldspar grains owing to the higher easiness for dissolving silicic acid in the former due to the presence of network modifiers which promote faster destruction of the Si-network through the ion exchange process.

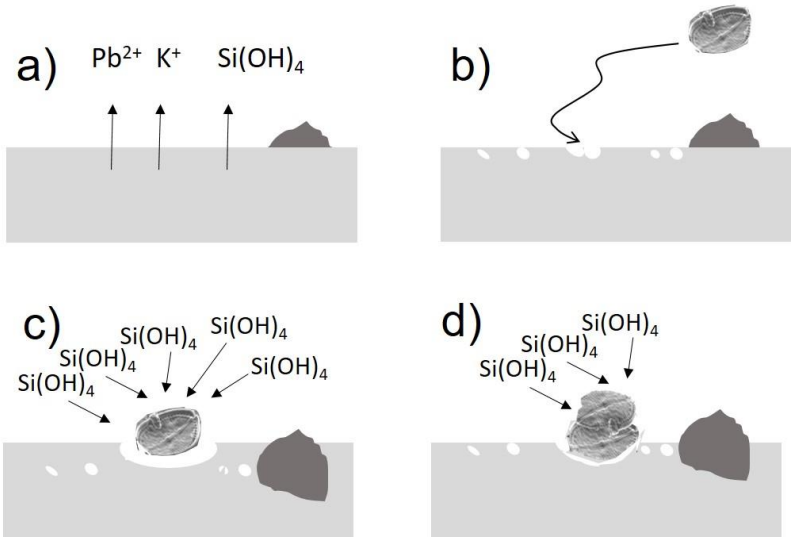

Figure 8.- Scheme of the growing of a diatom at expense of the glaze silica (grain of quartz or K-feldspar in dark grey, glassy matrix of glaze in light grey). a) ion exchange and hydrolysis processes dissolving ion network modifiers and silicic acid; b) formation of micropores on the glaze surface and young epitheca randomly deposited on a pore; c) growing of the diatom by silicification; d) concave socket molded from the glaze pore at expenses of the formation of the mature diatom.

4. Conclusions

The FIB-FESEM-EDX technique has been applied in the study of the corrosion processes of archaeological glazed ceramic for the first time. This advanced microscopy technique has been successful in the identification of corrosion layers of nanoscopic thickness and characterization of the nanomorphology that could not be identified using the conventional examination of cross-sections using FESEM-EDX. In addition, X-ray microanalysis carried out on the trenches has provided compositional data at the nanoscale that allow establishing a comparison between the chemical composition of the corrosion layer and the uncorroded glaze.

The three selected glazed ceramic pieces are good examples of the differential corrosion mechanisms that take place depending on the environmental conditions. The atmospheric environment promotes the formation of a thin precipitation layer formed by lead carbonates and deposited organic materials that have been degraded to oxalate salts. The

burial context has demonstrated a great degradative effect forming an amorphous gel layer that evolves to a thicker lamellar corrosion layer due to repeated seasonal humidity-dryness cycles. But the more interesting finding has been associated with the unusual and selective deteriorating effect on the marine matrix glaze due to the metabolic silicification activity of diatoms for forming their frustules during their growing and maturation. This effect has been reported for the first time in the present study.

Declaration of competing interest

The authors have declared no conflict of interest.

5. Acknowledgments

This work was supported by the Spanish R+D+I Project PID2020-113022GB-I00 supported by MCIN/ AEI/10.13039/501100011033. The authors wish to also thank Mr. Manuel Planes, Dr. José Luis Moya, and Alicia Nuez-Inbernón, technical supervisors of the Electron Microscopy Service of the *Universitat Politècnica de València*. Authors also aknowledge the support by Mr Joaquín Bolufer-Marqués, Director of the Museo Arqueológico y Etnografico Soler Blasco of Xàbia (Spain) and Mr. Josep Pérez-Camps director of the *Museo de Cerámica de Manises* (Spain).

6. References

[1] M.S. Tite, I. Freestone, R. Mason, J. Molera, M. Vendrell-Saz, N. Wood, Lead glazes in antiquity-methods of production and reasons for use, Archaeometry 40 (1998) 241-260. https:// 10.1111/j.1475-4754.1998.tb00836.x.

[2] T.M. El-Shamy, J. Lewins, R.W. Douglas, The dependence on the pH of the decomposition of glasses by aqueous solutions, Glass Technol. 13 (1972) 77-80.

[3] J.M. Fernández-Navarro, El Vidrio, CSIC, Madrid, 1991, pp. 590–591.

[4] B.C. Bunker, Molecular mechanisms for corrosion of silica and silicate glasses, J. Non-Cryst. Solids 179 (1994) 300-308. https:// 10.1016/0022-3093(94)90708-0.

[5] B. Lamain, M.R. Van Bommel, G. Verhaar, N.H. Tennent, The development of an ion chromatography protocol for detecting the early stages of glass degradation, in: K. Van Lokeren Campagne, H. Römich (Eds.), Recent Advances in Glass, Stained-Glass, and Ceramics Conservation, Amsterdam, 7–10 October 2013, SPA Uitgevers, Zwolle, 2013, pp. 303–311.

[6] A. Rodrigues, S. Fearn, T. Palomar, M. Vilarigues, Early stages of surface alteration of soda-rich-silicate glasses in the museum environment, Cor. Sci. 143 (2018) 362–375. https://doi.org/10.1016/j.corsci.2018.08.012.

[7] A. Rodrigues, S. Fearn, M. Vilarigues, Historic K-rich silicate glass surface alteration: Behaviour of high-silica content matrices, Cor. Sci. 145 (2018) 249–261. https://doi.org/10.1016/j.corsci.2018.10.010.

[8] T. Palomar, D. de la Fuente, M. Morcillo, M. Alvarez de Buergo, M. Vilariguesa, Early stages of glass alteration in the coastal atmosphere, Build. Environ. 147 (2019) 305–313. https://doi.org/10.1016/j.buildenv.2018.10.034.

[9] H. Römich, Historic glass and its interaction with the environment, in: Tennent NH (Ed.), The conservation of glass and ceramics, Research, practice and training, James & James, London, 1999, pp 5–14.

[10] M. Vilarigues, R.C. da Silva, Ion beam and infrared analysis of medieval stained glass, Appl. Phys. A 79 (2004) 373–378, https:// 10.1007/s00339-004-2538-9.

[11] N. Carmona, M.A. Villegas, J.M.F. Navarro, Characterisation of an intermediate decay phenomenon of historical glasses, J. Mater. Sci. 41 (2006) 2339–2346, https://10.1007/s10853-005-3948-6.

[12] C.M. Jackson, D. Greenfield, L.A. Howie, An assessment of compositional and morphological changes in model archaeological glasses in an acid burial matrix, Archaeometry 54 (2012) 489–507, https:// 10.1111/j.1475-4754.2011.00632.x.

[13] M. Melcher, M. Schreiner, Leaching studies on naturally weathered potash-lime-silica glasses, J. Non-Cryst. Solids 352 (5) (2006) 368–379, https:// 10.1016/j.jnoncrysol.2006.01.017.

[14] A. Genga, M. Siciliano, L. Famà, E. Filippo, T. Siciliano, A. Mangone, A. Traini, C. Laganara, Characterization of surface layers formed under natural environmental conditions on medieval glass from Siponto (Southern Italy), Mater. Chem. Phys. 111 (2008) 480–485. https://10.1016/j.matchemphys.2008.04.057

[15] T. Palomar, Characterization of the alteration processes of historical glasses on the Seabed, Mater. Chem. Phys. 214 (2018) 391-401. https:// 10.1016/j.matchemphys.2018.04.107.

[16] F. Barbana, R. Bertoncello, L. Milanese, C. Sad, Alteration and corrosion phenomena in Roman submerged glass fragments, J. Non-Cryst. Solids 337 (2004) 136–141. https://10.1016/j.jnoncrysol.2004.03.118.

[17] M. Schreiner**,** Corrosion of historic glass and enamels, Compr. Anal. Chem. 42 (2004) 713-754, https:// 10.1016/S0166-526X(04)80020-5.

[18] G.E. De Benedetto, P. Acquafredda, M. Masieri, G. Quarta, L. Sabbatini, P.G. Zambonin, M. Tite, M. Walton, Investigation on roman lead glaze from Canosa: results of chemical analyses, Archaeometry 46 (2004) 615–624, https://10.1111/j.1475-4754.2004.00177.x.

[19] E. Salinas, T. Pradell, The transition from lead transparent to tin-opacified glaze productions in the western Islamic lands: al-Andalus, c. 875–929 CE, J. Archaeol. Sci. 94 (2018) 1-11, https://10.1016/j.jas.2018.03.010, and references therein.

[20] J. Molera, M. Vendrell-Saz, J. Pérez-Arantegui, Chemical and Textural Characterization of Tin Glazes in Islamic Ceramics from Eastern Spain, J. Archaeol. Sci. 28 (2001) 331-340, https://10.1006/jasc.2000.0606.

[21] A. Machado, M. Vilarigues, Blue enamel pigment-Chemical and morphological characterization of its corrosion process, Cor. Sci. 139 (2018) 235–242, https://10.1016/j.corsci.2018.05.005.

[22] X. Yin, T.J. Huang, H. Gong, Chemical evolution of lead in ancient artifacts -A case study of early Chinese lead-silicate glaze, J. Eur. Ceram. Soc. 40 (2020) 2222-2228, https:// 10.1016/j.jeurceramsoc.2020.01.002.

[23] Y. Zhou, Y. Hu, Y. Tao, J. Sun, Y. Cui, K. Wang, D. Hu, Study on the microstructure of the multilayer glaze of the16th-17th century export blue-and-white porcelain excavated from Nan'ao-I Shipwreck, Ceram. Int. 42 (2016) 17456–17465, https:// 10.1016/j.ceramint.2016.08.050.

[24] A. Doménech-Carbó, M.T. Doménech-Carbó, J.V. Gimeno-Adelantado, M. Moya-Moreno, y F. Bosch-Reig, Identification of lead (II) and (IV) in mediaeval glazes by cyclic voltammetry and differential pulse voltammetry. Application to the study of alterations in archaeological ceramic, Electroanalysis, 12 (2000) 120-127, https:// 10.1002/(SICI)1521-4109(200002)12:2<120.

[25] A. Doménech-Carbó, M.T. Doménech-Carbó Electrochemical Characterization of Archaeological Tin-Opacified Lead-Alkali Glazes and Their Corrosion Processes, Electroanalysis 17 (2005) 1959–1969, https:// 10.1002/elan.200503322.

[26] M.T. Doménech-Carbó, A. Doménech-Carbó, L. Osete-Cortina, M.C. Saurí-Peris, A Study on Corrosion Processes of Archaeological Glass from the Valencian Region (Spain) and its Consolidation Treatment, Mikrochim. Acta, 154 (2006) 123-142, https:// 10.1007/s00604-005-0472-y.

[27] A. Doménech-Carbó, M.A. Villegas, F. Agua, M.T. Doménech-Carbó, B. Martínez-Ramírez, Electrochemical fingerprint of archaeological lead silicate glasses from the voltammetry of microparticles approach, J. Am. Ceram. Soc., 99 (2016) 3915-3923, https://10.1111/jace.14430.

[28] J. Roqué-Rosell, A. Pinto, C. Marini, J. Prieto Burgos, J. Groenen, M. Campeny, Ph. Sciau, Synchrotron XAS study of Mn and Fe in Chinese blue-and-white Ming porcelains from the second half of the 15th century, Ceram. Int. 47 (2021) 2715–2724, https://doi.org/10.1016/j.ceramint.2020.09.123.

[29] C. De Vito, L. Medeghini, S. Garruto, F. Coletti, I. De Luca, S. Mignardia, Medieval glazed ceramic from Caesar's Forum (Rome, Italy): Production technology, Ceram. Int. 44 (2018) 5055–5062, https://doi.org/10.1016/j.ceramint.2017.12.104.

[30] S. Polić, S.Ristić, J.Stašić, M.Trtica, B.Radojković Studies of the Iranian medieval ceramic surface modified by pulsed tea CO2 and Nd:YAG lasers, Ceram. Int. 41 (2015) 85-100, http://dx.doi.org/10.1016/j.ceramint.2014.08.036.

[31] J. Wen, Z. Chen, Q. Zeng, L. Hu, B. Wang, J. Shi, G. Zhang, Multi-micro analytical studies of blue-and-white porcelain (Ming dynasty) excavated from Shuangchuan island, Ceram. Int. 45 (2019) 13362–13368, https://doi.org/10.1016/j.ceramint.2019.04.031.

[32] Y. Xu, Y. Qin, F. Ding, Characterization of the rare oil spot glazed bowl excavated from the Xiao kiln site of north China, Ceram. Int. 43 (2017) 8636-8642, http://dx.doi.org/10.1016/j.ceramint.2017.03.177.

[33] R. Zhang, I. Garachon, P. Gethin, J. van Campen, Double layers glaze analysis of the Fujian export blue-and-white porcelain from the *Witte Leeuw* shipwreck (1613), Ceram. Int. 46 (2020) 13474-13481, https://doi.org/10.1016/j.ceramint.2020.02.131.

[34] S. Saber-Samandari, K. Alamara, S. Saber-Samandaric, Calcium phosphate coatings: Morphology, micro-structure and mechanical properties, Ceram. Int. 40 (2014) 563-572, http://dx.doi.org/10.1016/j.ceramint.2013.06.038.

[35] H. Berek, C.G. Aneziris, Effect of focused ion beam sample preparation on the phase composition of zirconia, Ceram. Int. 44 (2018) 17643–17654, https://doi.org/10.1016/j.ceramint.2018.06.226.

[36] T. Pradell, R. Fernandes, G. Molina, A.D. Smith, J. Molera, A. Climent-Font, M.S. Tite, Technology of production of Syrian lustre (11th to 13th century), J. Eur. Ceram. Soc. 38 (2018) 2716–2727, https://doi.org/10.1016/j.jeurceramsoc.2018.01.046.

[37] G. Molina, M.S. Tite, J. Molera, A. Climent-Font, T. Pradell, Technology of production of polychrome lustre, J. Eur. Ceram. Soc. 34 (2014) 2563–2574, http://dx.doi.org/10.1016/j.jeurceramsoc.2014.03.010.

[38] M.T. Doménech-Carbó, F. di Turo, N. Montoya, F. Catalli, A. Doménech-Carbó, C. de Vito, FIB-FESEM and EMPA results on Antoninianus silver coins for manufacturing and corrosion processes, Sci. Rep. 8 (2018) 10676, https://10.1038/s41598-018-28990-x

[39] M.T. Doménech-Carbó, C. Álvarez-Romero, A. Doménech-Carbó, L. Osete-Cortina, M. L. Martínez-Bazán, Microchemical surface analysis of historic copper-based coins by the combined use of FIB-FESEM-EDX, OM, FTIR spectroscopy and solid-state

electrochemical techniques, Microchem. J. 148 (2019) 573-581, https:// 10.1016/j.microc.2019.05.039.

[40] M.T. Doménech-Carbó, Y. Lee, L. Osete-Cortina, S. Marín-Rey. Influence of plasticizer and biocide on the functional properties of gelatin-based adhesives used in painting consolidation, J. Adhes. Sci. Technol. 29 (2015) 1774-1795, https:// 10.1080/01694243.2014.975999.

[41] S. Amma, S.H. Kim, C.G. Pantano, Analysis of Water and Hydroxyl Species in Soda Lime Glass Surfaces Using Attenuated Total Reflection (ATR)-IR Spectroscopy, J. Am. Ceram. Soc. 99 (2016) 128–134. https:// 10.1111/jace.13856.

[42] F.H. El-Batal, E.M.A. Khalil, Y.M. Hamdy, H.M. Zidan, M.S. Aziz, A.M. Abdelghany, Infrared reflection spectroscopy for precise tracking of corrosion behavior in 3D-transition metals doped binary lead silicate glass, Physica B 405 (2010) 2648–2653, https://doi.org/10.1016/j.physb.2010.03.044.

[43] C. Bonnet, A. Bouquillon, S. Turrell, V. Deram, B. Mille, J. Salomon, J.H. Thomassin, C. Fiaud, Alteration of lead silicate glasses due to leaching in heated acid solutions, J. Non-Cryst. Solids, 323 (2003) 214–220, https://10.1016/S0022-3093(03)00279-5.

[44] G. Li, H. Ji, Ch. Lv, N. Li, Y. Hong, L. Zhang, Aging study on the modern imitation glaze and ancient glaze of the Ming and Qing dynasties based on FTIR decomposition spectra, J. Non-Cryst. Solids 505 (2019) 102–108, https://: doi.org/10.1016/j.jnoncrysol.2018.10.024

[45] M. Sitarz, The structure of simple silicate glasses in the light of Middle Infrared spectroscopy studies, J. Non-Cryst. Solids 357 (2011) 1603–1608, https://10.1016/j.jnoncrysol.2011.01.007.

[46] C.A. Worrell, T. Henshall, Vibrational spectroscopic studies of some lead silicate glasses, J. Non-Cryst. Solids 29 (1978) 283-299, https:// 10.1016/0022-3093(78)90150-3.

[47] R. Ali Rahimi, S.K. Sadrnezhaad, G. Raisali, Chemical durability of lead silicate glass in HNO_3, HCl and H_2SO_4 aqueous acid solutions, J. Non-Cryst. Solids 355 (2009) 169–174. https://doi.org/10.1016/j.jnoncrysol.2008.11.001.

[48] M. Vilarigues, P. Redola, A. Machado, P.A. Rodrigues, L.C. Alves, R.C. da Silva Corrosion of 15th and early 16th century stained glass from the monastery of Batalha studied with external ion beam, Mater. Charact. 62 (2011) 211-217, https://doi.org/10.1016/j.matchar.2010.12.001.

[49] A. Xie, Y. Shen, D. Ma, F. Huang, L. Qiu, S. LiL. Chen, Growth of calcium oxalate crystals induced by complex films containing biomolecules, Cryst. Res. Technol. 42 (2007) 667–72, https:// 10.1002/crat.200610886.

[50] C. Schultz-Münzenberg, W. Meisel, P. Gütlich, Changes of lead silicate glasses induced by leaching, J. Non-Cryst. Solids, 238 (1998) 83-90, https://doi.org/10.1016/S0022-3093(98)00580-8.

[51] R. Bertoncello, L. Milanese, A. Bouquillon, J.-C. Dran, B. Mille, J. Salomon, Leaching of lead silicate glasses in acid environment: compositional and structural changes, Appl. Phys. A 79 (2004) 193–198, https:// 10.1007/s00339-004-2651-9.

[52] R.K. Iler, The Chemistry of Silica: Solubility, Polymerization, Colloid and Surface Properties, and Biochemistry, Wiley-Interscience, New York, 1979.

[53] M. Hildebrand, S.J.L. Lerch, R.P. Shrestha, Understanding Diatom Cell Wall Silicification—Moving Forward, Front. Mar. Sci. 5 (2018) 125, https:// 10.3389/fmars.2018.00125.

Declaration of interests

☒ The authors declare that they have no known competing financial interests or personal relationships that could have appeared to influence the work reported in this paper.

☐The authors declare the following financial interests/personal relationships which may be considered as potential competing interests:
